Detection of hydration on nominally anhydrous S-complex Main Belt Asteroids

Maggie McAdam[1], Cristina Thomas[2], Lauren McGraw[2], Andrew Rivkin[3], Joshua Emery[2]

[1]NASA Ames Research Center.
[2]Northern Arizona University.
[3]Johns Hopkins University's Applied Physics Laboratory.

Abstract

We present the results of a survey of nominally anhydrous Main Belt S-complex asteroids. Thirty-three observations of 29 unique asteroids were obtained using the IRTF+SpeX instrument in prism and LXD short modes. We report for the first time that S-complex main belt asteroids have 3-µm features. The majority of the observations (27 of 33) have a detectable 3-µm feature that is at least 1% band depth or greater (within error), indicating the presence of hydration. Most of the asteroids have bands of 1 – 2.5% depth but a notable fraction (9 of the observations) have band depths of >5%. These band depths are comparable with low albedo asteroids in the mid and outer belt that experienced aqueous alteration. We investigate the origin of the hydration, searching for correlations with orbital, physical and circumstantial parameters. However, we do not find any strong or moderate correlations with 3-µm band depth, indicating multiple factors may be at play, including exogenic sources, primordial water and/or solar wind implantation. Additionally, we report the mineralogies of the asteroids, derived from the prism observations.

1 - Introduction:

In our Solar System, we observe two broadly defined regions characterized by the abundance of water: the icy outer Solar System with less abundant rocky materials and the inner Solar System characterized by a greater abundance of rocky materials and less abundant volatiles, especially water. This is not to say that the inner Solar System has no water, but rather that the water observed on planets and small bodies interior to Jupiter's orbit represents a much lower proportion of the materials compared to the outer Solar System bodies like comets, trans-Neptunian objects and icy moons.

Water is present on every planet in the inner Solar System (e.g., Lawrence et al., 2013, Donahue and Hodges, 1993, Wordsworth, 2016; Wray, 2021), including the moon (e.g., Pieters et al., 2009; Clark, 2009; Sunshine et al., 2009; Honniball et al., 2020; Honniball et al., 2022). Water and hydroxyl found in the inner Solar System may be formed in-situ (e.g., Honniball et al., 2020), delivered to the surface (e.g., Brenna et a., 2019) or created on the surface through interactions with the solar wind (e.g., Hibbitts et al., 2011) Evidence of water has also been observed on asteroids.

In the Main Asteroid Belt, evidence of water ice and organics has been inferred by bowl-shaped 3-µm features (e.g., Rivkin and Emery, 2010; Campins et al., 2010; Takir and Emery, 2012). Other evidence of water has been seen on Ceres, which is thought to have experienced extensive interactions with coaccreted water (e.g., De Sanctis et al., 2020). Psyche and other M-types have also been observed to have the signature of hydration around 3-µm (Jones et al., 1990; Rivkin et al., 2000; Landsman et al., 2015; Takir et al., 2017). Similarly, remote observations of Vesta indicate the presence of a 3-µm band (e.g., Hasegawa et al., 2003; McGraw et al., 2022). Observations made by the Dawn mission indicate that the enhanced signature of hydrogen from gamma ray neutron spectral observations are not merely caused by solar wind implantation (Prettyman et al., 2015). Dawn results also find evidence of dark exogenic material on Vesta's surface which likely causes the weak 3-µm feature observed in Vesta's spectrum (e.g., McCord et al., 2012; Reddy et al., 2012; Hasegawa et al., 2003; McGraw et al., 2022). In near-Earth space, 3-µm features have been detected on Eros and Ganymed, two of the largest near-Earth objects (e.g., Rivkin et al., 2018). McGraw et al. (2022) also presented a survey of NEAs showing more detections of 3-µm features which could be caused by implanted OH from solar wind or exogenic material similar to Vesta. Finally, Galileo observations of the S-type Gaspra also indicate the presence of hydration (e.g., Granahan et al., 1994; Granahan et al., 2011).

Main belt S-complex asteroids, as a taxonomic class, have not been systematically observed to search for evidence of hydration (water-ice, hydroxyl in hydrated minerals. In fact, S-complex asteroids have always been assumed to be dry; that is that they do not contain water or at least a negligible abundance of water at the time of accretion. Without significant water at the time of accretion, S-complex asteroids do not have significant phyllosilicates like C-complex asteroids. S-complex asteroids are assumed to be dry because they formed in the inner Solar System like the terrestrial planets (e.g., Bell et al., 1989; Raymond et al., 2020; Izidoro et al., 2023; Deienno et al., 2023). However, evidence in meteorites suggests that even anhydrous groups, including ordinary chondrites, have detectable water in them (e.g., Wood, 2005). Given the observations from ordinary chondrites which are thought to be linked to S-type asteroids, as well as the pervasive detection of hydration across many anhydrous asteroids including Vesta and Psyche, we prepared an investigation of S-complex asteroids searching for 3-µm features.

In this study, we investigate both the evidence of hydration, through 3-µm spectroscopy on nominally anhydrous inner and mid Main Belt S-type asteroids as well as its potential origin. Here 'hydration' is defined as the detection of a 3-µm feature that is produced by the fundamental vibration of O-H bonds in hydroxyl and/or water. In the 3-µm wavelength region, water (H_2O molecules) and hydroxyl (OH molecules) share a degenerate vibrational mode. We cannot distinguish between OH and H_2O using this wavelength region alone but the presence of a 3-µm band is indicative of OH/H_2O. The signature of hydration can be caused by hydrated minerals (such as phyllosilicates) that are endogenic to the object, OH created on grain surfaces through interactions with solar wind, and/or exogenic hydrated minerals brought to an object through impacts.

We present a large study of 29 nominally anhydrous S-type asteroids using near-infrared spectral observations using NASA's Infrared Telescope Facility's SpeX instrument in the prism(0.7 – 2.5-μm) and LXD-short (1.67 – 4.2-μm) to investigate whether these objects show the telltale hydration absorption in this region as well as their underlying silicate mineralogy. This dataset, representing hundreds of hours of observing time, is the starting place to investigate the pervasive presence of water throughout the main asteroid belt. We will present our dataset and potential explanations for the hydration on these S-type asteroids.

2 - Observations and Data Reduction

2.1 – Observations

We were awarded 30 observing runs with IRTF between February 2017 and May 2020. Over these nights, we obtained 34 observations of 29 unique S-type asteroids. We used the SpeX instrument (Rayner et al., 2003) for these observations in both the prism (0.7-2.52-μm, R~200) and LXD short modes (1.67-4.2-μm, R~2500). Our observations were made using the 0.8 arcsecond slit. In general, we observed each object using the prism and LXD modes on the same night of observing. A few of the asteroids were only observed with the LXD mode and one had a prism spectrum taken on a different night. Integration times, co-adds and total exposure times were chosen based on the asteroid's brightness and the weather conditions. Particularly in prism mode, the exposure times vary due to the brightness of the objects in this study. A summary of the asteroids, dates, observing circumstances, total exposure time and standard stars are listed in **Table 1**.

Standard stars were selected in two ways. Often, we used Bobby Bus's standard star list from SMASS observations (Burbine and Binzel, 2002). Additionally, we searched for solar-like standard stars in the SIMBAD database within a 4^{o} radius around the asteroid's position on the night of observation to ensure a good telluric match for the LXD reduction process. The closest G star in the sky with B-V and V-K colors most similar to the Sun was selected.

2.2 - Reduction

2.2.1. Prism data reduction:

After the data were collected, they were reduced using the IDL Spextool package (Cushing et al., 2004; Vacca et al., 2003). Each image was first extracted using Spextool. Telluric corrections were done with an ATRAN-based code (MacLennan, 2019) then the tellurically corrected data were combined into a single spectrum for analysis. The prism data and derived mineralogy are discussed in **Section 3.1** and **Appendix 1,** respectively**.**

2.2.2 LXD data reduction

The LXD spectra were extracted using Spextool, corrected for telluric contamination with the basic telluric correction package that divides by the contemporaneous standard star observations, then combined and merged into a single spectrum. We followed the process presented in McGraw et al., (2022) of frequent standard star observations. This package provides flat field correction and wavelength calibrations to extract the spectra. Standard stars and asteroids were extracted using the same process, then the standards observed at similar airmasses were used to remove telluric contamination. The data between 2.55-2.85-μm is excluded because the atmosphere is opaque in this region due to the absorption of atmospheric water.

After first processing all of the data in this manner, we noted that several (11 objects) had a persistent artifact in their spectra. This appeared as a bump around 3.5-μm. This feature is caused by the sensitivity drop-off at the edges of the LXD orders around 3.5-μm. As a consequence, the object tracing algorithm failed to properly find the object's location in the slit during the initial extraction step. When the orders were subsequently merged, the 3.5-μm bump artifact appeared because there was not sufficient signal in the orders to adequately combine the data, resulting in the bump artifact. To solve this problem, we re-reduced the asteroid data by first combining the images (which enhances the signal at all wavelengths), then performing the flat field, wavelength calibrations and extraction steps. Data were then tellurically corrected and merged to create a final spectrum used for analysis. When the spectra are combined first, there are sufficient signal-to-noise in each order to allow the tracing algorithm to accurately find and trace the object in the slit.

2.3 - Thermal Modeling

In the LXD wavelength region, asteroids exhibit a thermal excess caused by the blackbody re-radiation of the asteroid itself. Depending on the temperature of the asteroid, the thermal excess can be significant and obscure underlying mineralogy and/or signature of hydration (if present) in the ~2.8-4.2-μm region. We utilize a thermal modeling code based on the Near-Earth Asteroid Thermal Model (Harris, 1998) to remove the thermal excess.

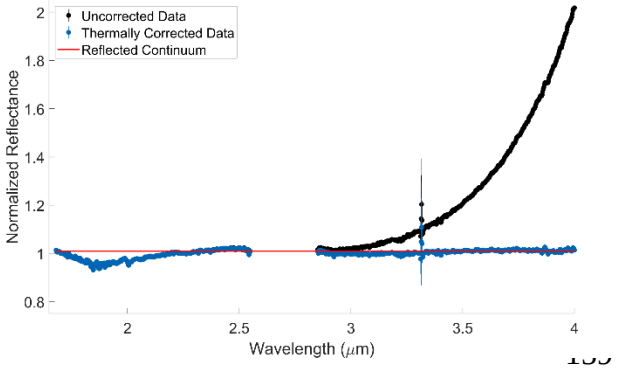

Figure 1: Example of an uncorrected LXD spectrum, reflected continuum, and thermally corrected data.

The LXD spectra cover the K and L bands (2-2.4-μm and 3-4-μm, respectively). In the thermal model code, we assume that thermal excess is all in the K (~2-2.5-μm) and L band (~3-4-μm). The thermal excess is then modeled based on the asteroid's phase angle, size, albedo and relative position to the Sun (r_H) and Earth (Δ). We then subtract off combined thermal continuum thus removing the contribution from the blackbody radiation

of the asteroid. **Figure 1** shows an example of a spectrum, thermal model, and thermally corrected data.

Separately, we also calculate the instantaneous theoretical equilibrium temperature of each object. We calculate this quantity with this equation:

$$T_{eq} = \left[\frac{(1-A_B)F_{Sun}}{(0.756 \cdot \varepsilon \cdot \sigma) \cdot r_H^2}\right]^{\frac{1}{4}}.$$

F_{Sun} is the flux of the Sun at 1 au (1365 W/m^2), ε is the infrared emissivity set to a value of 0.9, and σ is the Stephan-Boltzmann constant (5.67x10^{-8} W m^{-2} K^{-4}). The parameter r_H is the instantaneous heliocentric distance for each object at the time of observation. A_B is the Bond albedo. For asteroids, we use the treatment of Bowell et al., (1989) to calculate this quantity:

$$A_B = pv \cdot (0.290 + 0.684 \cdot G),$$

where pv is the geometric albedo in the visible wavelengths and G is the magnitude slope (both values are taken from Horizons[1] for each asteroid).

The thermal model parameters and the equilibrium temperature for each asteroid are listed in **Table 2**. Thermally corrected data appear in **Section 3.4**.

2.4 - Asteroids physical and orbital characteristics

We gathered a number of physical and orbital parameters for each asteroid observed in this work. These include absolute magnitude, albedo, diameter, rotation period, semi-major axis, perihelion and aphelion distances and spectral taxonomic type(s). All of these parameters were gathered from the JPL Horizons database. In addition to the orbital and physical parameters, we also used the asteroid spectrum classification tool[2] to produce principal component analysis of our near-infrared spectra. This webtool uses the Bus-DeMeo taxonomy framework (DeMeo et al., 2009) and the tool itself was developed at MIT by Stephen Slivan. We are primarily concerned the slope of the spectrum. The other principal components are included in the Appendix. All of the quantities used in the subsequent sections can be found in **Table 3**.

3 - Previous Observations of Asteroids in this study

[1] https://ssd.jpl.nasa.gov/horizons/
[2] http://smass.mit.edu/cgi-bin/busdemeoclass-cgi

The majority of the asteroids in this study have taxonomic classifications but do not have reported interpretations of their near-infrared or 3-µm spectroscopy [including: (5) Astrea, (30) Urania, (33) Polyhymnia, (39) Laetita, (67) Asia, (103) Hera, (115) Thyra, (151) Abunditia, (182) Elsa, (208) Lacrimosa, (277) Elvira, (352) Gisela, (462) Eriphyla, (703) Noemi, and (913) Otila]. Nine of the asteroids presented in this work have been previously studied using near-infrared spectroscopy (e.g., (3) Juno: Degewij et al., 1979; Sinokawa et al., 2002, Noonan et al., 2019; (6) Hebe Chapman et al., 1973, Migilorini et al., 1997, Broglia et al., 1994; (7) Iris: Noonan et al., 2019, Vernazza et al., 2010; (8) Flora: Cloutis et al., 1990; (9) Metis: Marchis et al., 2006, Kelley and Gaffey, 2000; (11) Parthenope: Vernazza et al., 2010; (808) Merxia and (17) Thetis: Sunshine et al., 2004; (364) Isara: Vernazza et al., 2010). Gaffey et al., 1993 also reported the near-infrared spectra of a large number of the objects observed in this work. All previous analyses are consistent with a nominally anhydrous composition.

For the purposes of this paper, we are primarily interested in the asteroid's potential hydration state. Only two asteroids (Hebe and Flora) have been previously observed with 3-µm spectroscopy. Rivkin et al., (2001) report observations of (6) Hebe. Rivkin and coauthors suggested that there are variations across Hebe's surface in 3-µm band depth and that Hebe may be an aqueously altered body. Observations of (8) Flora presented in Eaton et al., (1983) do not indicate evidence of hydration.

4 - Results

4.1 - Near-infrared spectra

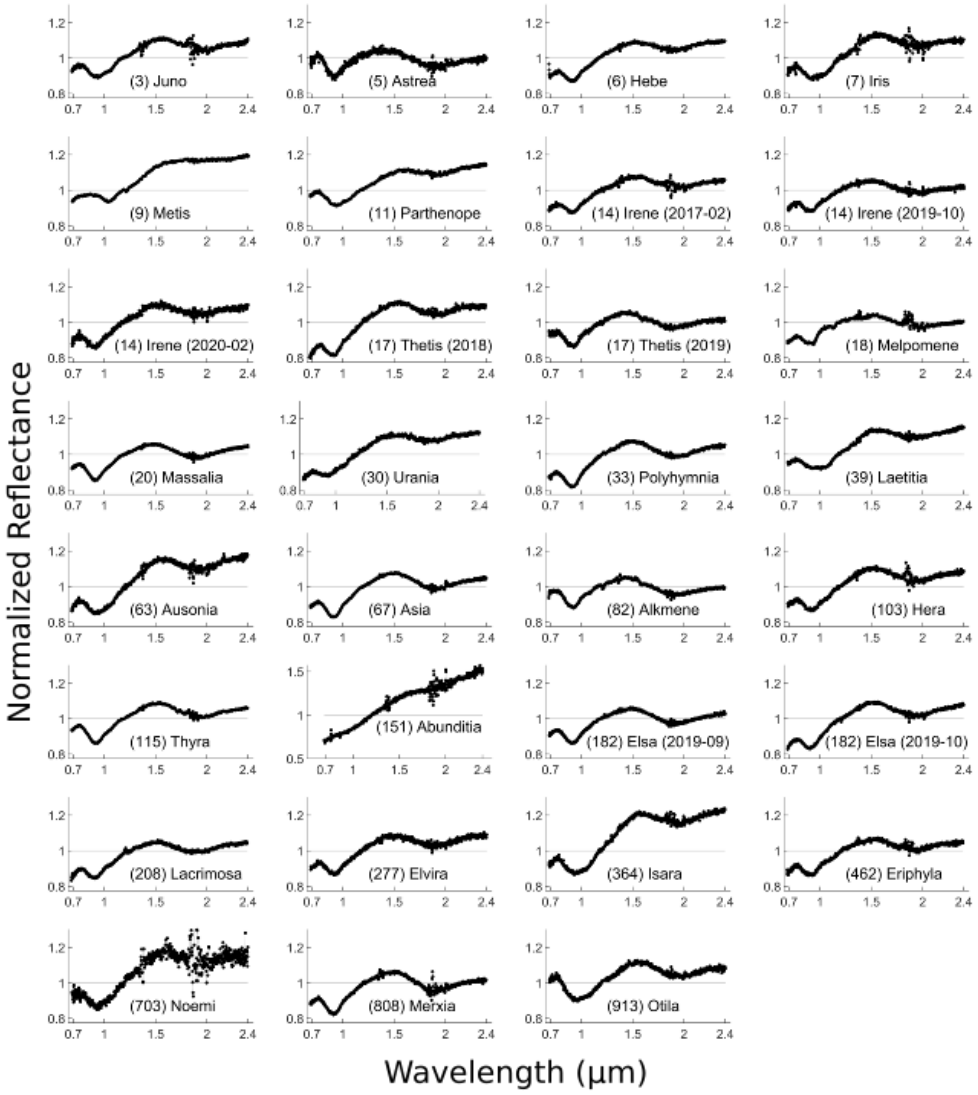

Figure 2: Near-infrared data of the observed asteroids.

Presented in **Figure 2** are the near-infrared spectra for each object in this study. All of the asteroids classify in the S-complex. The prism mode of the IRTF+SpeX instrument covers the wavelength range from ~0.7 – 2.5-μm. Further discussion of the near-infrared data, including derivation and interpretation of mineralogy can be found in **Appendix 1**.

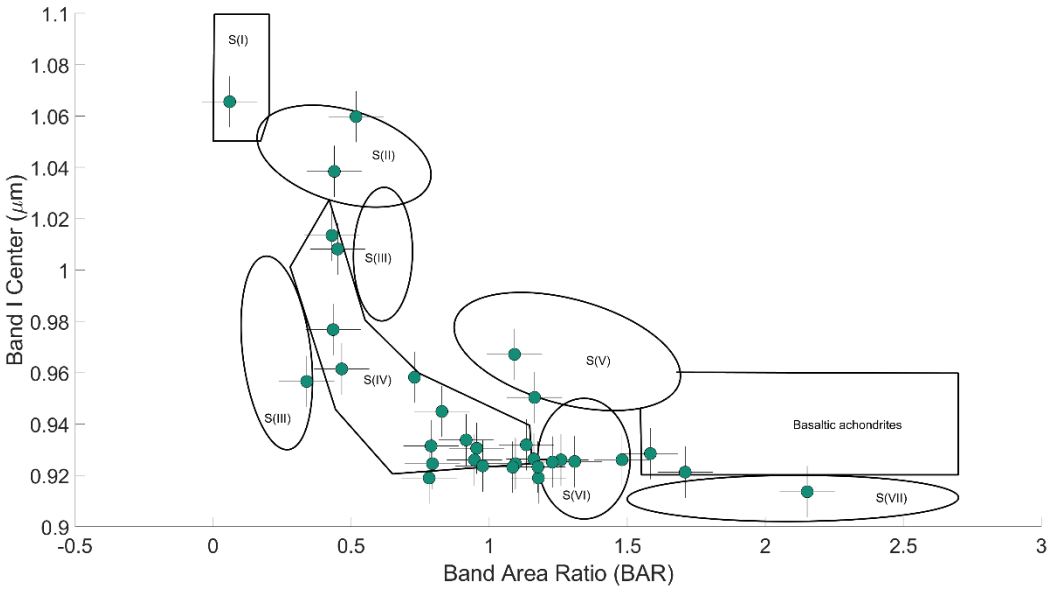

Figure 3: Band Area Ratio vs. Band I center (Gaffey plot). Here we present the results of the band parameter analysis and S-type subclasses based on the Gaffey (1993) plot. The nominally anhydrous asteroids we observed exhibit a wide variety of mineralogy from olivine dominated to basaltic achondrites. The majority of the objects are classified as SIV (ordinary chondrite boot) and SVI subtypes.

Using the results from the band parameter analysis described in **Appendix 1**, we assess the mineralogy of our sample. We impose minimum errors of 0.01 for band center, and 0.1 for band area ratio (BAR) to account for systematic errors in the data, consistent with Thomas et al., 2014 and references therein. In **Figure 3**, we present the "Gaffey plot" of Band I center vs BAR. We over plot our data with the S-type subclasses presented in Gaffey et al., (1993).

The S-complex asteroids observed in this work exhibit a wide range of mineralogies from olivine dominated to basaltic achondrite mineralogy. The majority (17/33) of the observations are consistent with the S(IV) subclass which is also referred to as the 'ordinary chondrite boot'. Asteroids in this particular field are consistent with ordinary chondrites (Gaffey et al., 1993) and potentially partially differentiated primitive achondrites (e.g., Lucas et al., 2019).

Descriptions of the mineralogy inferred from the band parameter analysis of the near-infrared spectra for all the asteroids in this study are presented in **Table 4**.

4.2 - 3-µm Spectroscopy of sample

The thermally corrected LXD spectra of the asteroids in this sample are presented in **Figure 4**. The LXD spectra of the S-type asteroids observed in this work show an absorption band with a flat shape between 2.9-3.4-µm. Mid- and outer-main belt asteroids with significant hydration typically exhibit either checkmark-like features or bowl-like features. The S-complex asteroids

are spectrally distinct from low albedo objects. Similarly, they are generally distinct from nominally anhydrous near-Earth asteroids also observed in the 3-µm region (McGraw et al., 2022). McGraw et al. presented spectra of S- and Q-type near-Earth asteroids showing a variety of band shapes. This is discussed further in **Section 5.2**.

4.2.1 - 3-µm band depth Methodology:

After thermally modeling each asteroid's LXD data (described in **Section 2.3**), the band depth for each object is determined. To do this we take the mean of the data (rb) and the reflected continuum (rc) within 3.0-µm +/- 0.025-µm. The 3.0-µm band depth is defined as the difference between the averaged continuum values and the averaged data values divided by the averaged continuum values:

$$band\ depth = \frac{(rc-rb)}{rc}.$$

Error is estimated as the standard deviation of the spectrum at 3.0 +/- 0.025-µm.

4.3 - 3-µm Band Depths

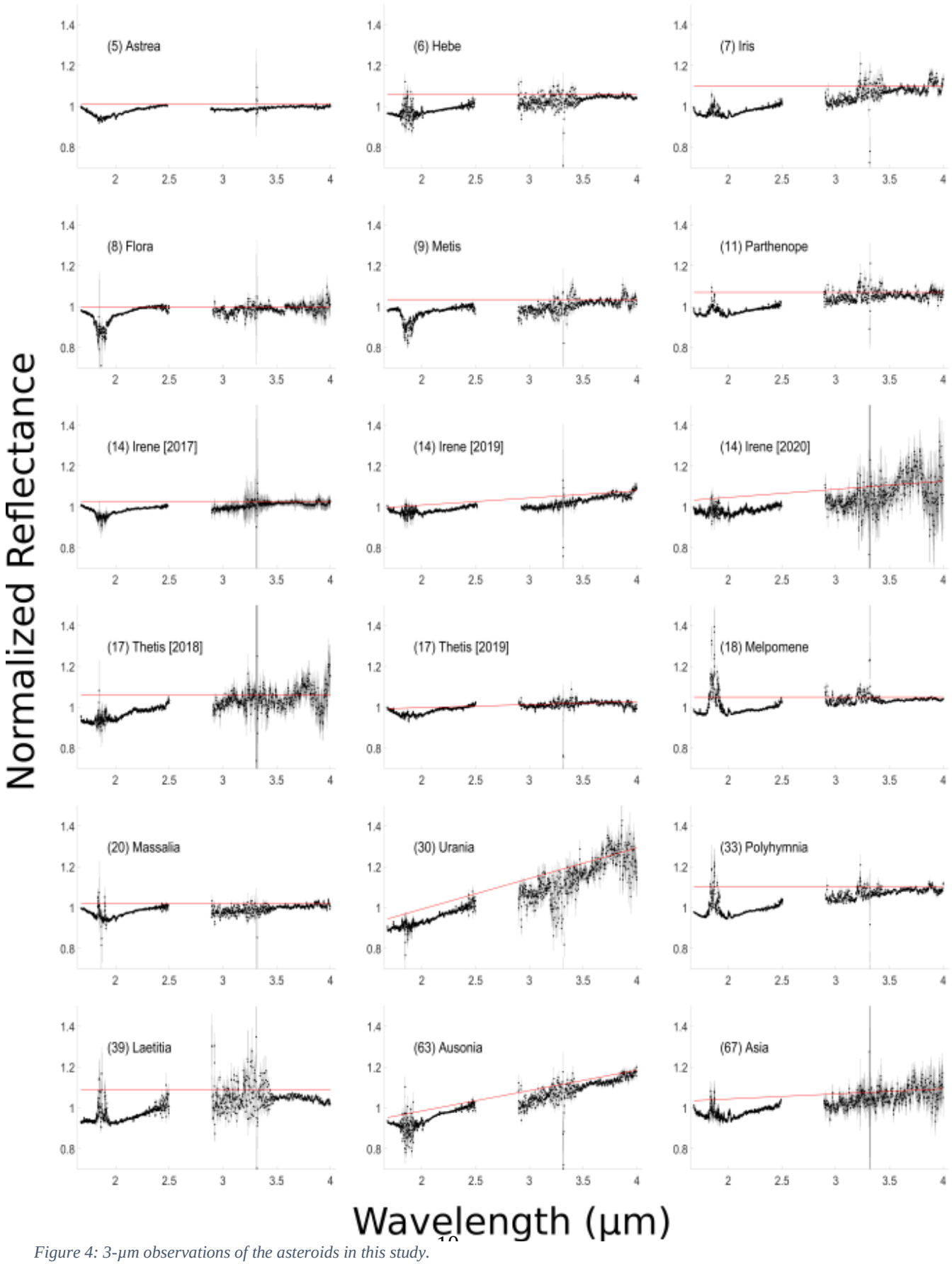

Figure 4: 3-μm observations of the asteroids in this study.

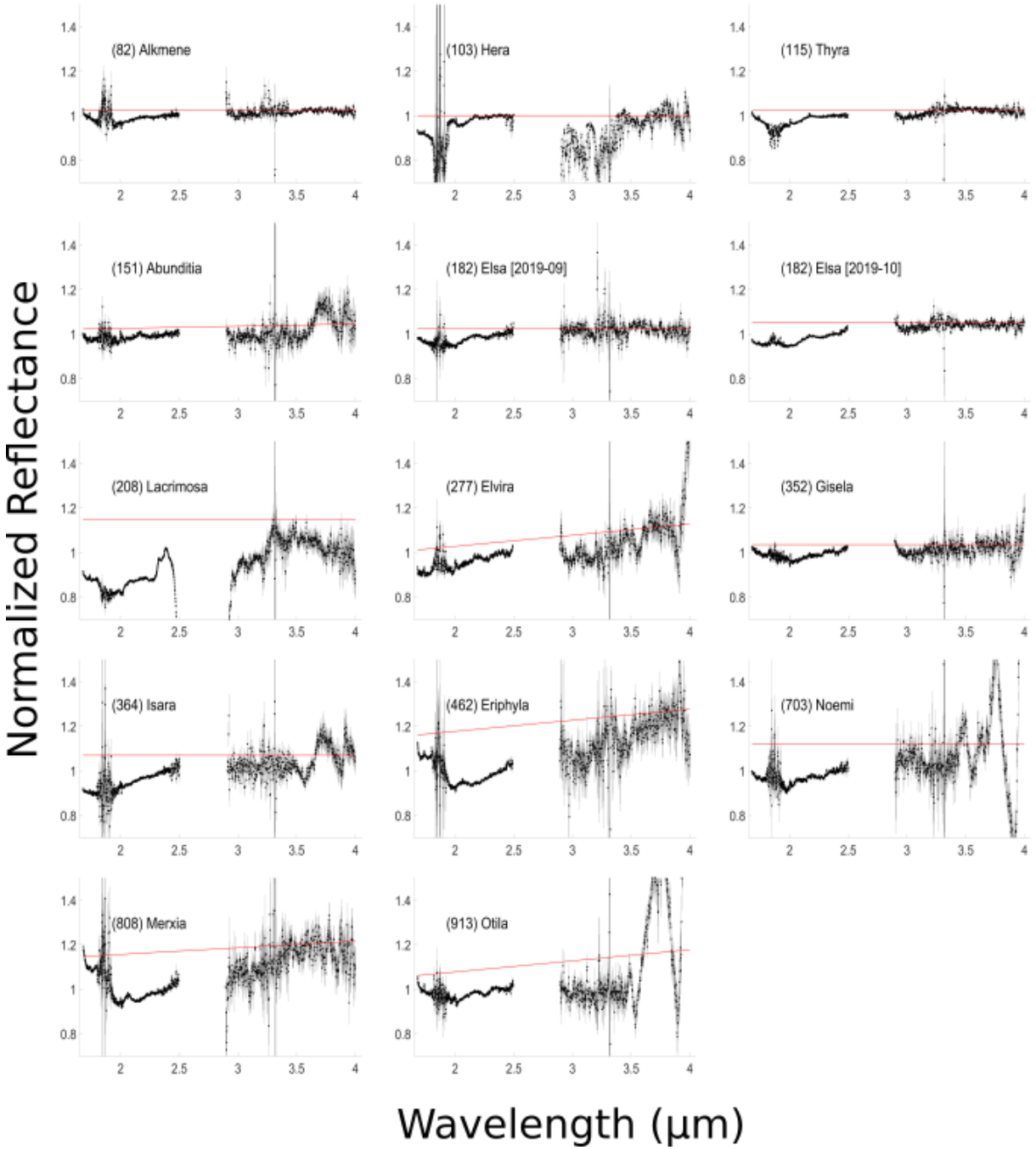

Figure 4 continued: 3-μm observations of the asteroids in this study.

4.3.2 - 3-µm Band Depth Results:

The 3-µm band depths for the objects in this study are presented in **Table 5**. For the 33 LXD observations of the 29 objects reported in this study, we find that all but 6 of the asteroids have a detectable 3.0-µm band of ≳1% depth within the error of the measurement. Band depths for the observed S-type asteroids range from ~1.8+/- 0.11% to 12.5 +/-1.5%. This indicates the presence of OH/H_2O on the surfaces of 23 nominally anhydrous S-type asteroids within error. Given our current understanding of the presence of water on the surfaces of 'dry' airless bodies like the moon (Pieters et al., 2009; Clark, 2009; Sunshine et al., 2009) and near-Earth objects (e.g., McGraw et al., 2022), this result may not be surprising, however, several of these objects have unexpectedly deep 3.0-µm bands.

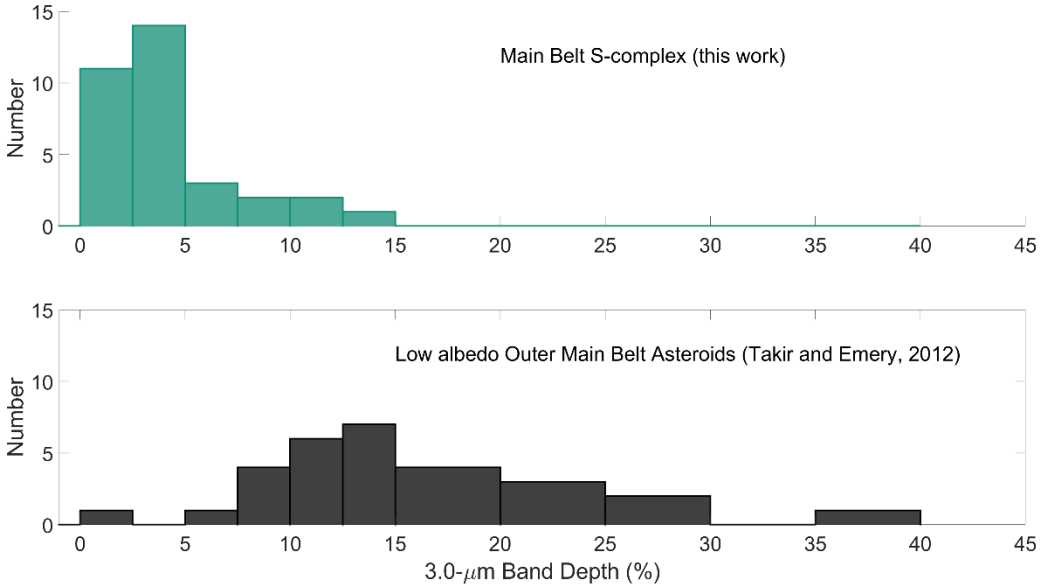

Figure 5: Figure 5: Histogram of 3-µm band depths for the nominally anhydrous S-complex asteroids (top) and values from low-albedo mid- and outer-main belt asteroids from Takir and Emery (2012). Some of the S-complex asteroids studied in this work have 3-µm band depths that are consistent with hydrated asteroids.

Nine of the 29 objects have 3.0-µm band depths of ≳5% depth with three asteroids ≳ 10% band depths. Surprisingly, these deeper 3.0-µm band depths are consistent with the 3.0-µm band depths reported for hydrated low albedo asteroids in the mid- and outer-main belt (**Figure 5**; Takir and Emery, 2012).

4.3.3 OH/H_2O Band Depth Discussion

Hebe is known to have surface heterogeneity (e.g., Chapman et al., 1973; Migilorini et al., 1997; Broglia et al., 1994). Rivkin et al. (2001) presented two 3-µm spectra of Hebe where they also

saw differences in 3-µm band depth. The 3-µm spectrum presented here does not have a detectable band (e.g., ~1.7 ± 1.8%). It seems that we observed the part of Hebe's surface with minimal hydration rather than the part of the surface with more significant hydration from Rivkin et al. (2001). Our spectrum is visually consistent with the 'less-hydrated' Hebe spectrum from Rivkin et al. (2001).

Arredondo et al. (2024) investigated four of the asteroids presented here using mid-infrared spectroscopy from the Stratospheric Observatory for Infrared Astronomy covering 4.9 – 13.7-µm [(7) Iris, (11) Parthenope, (18) Melpomene, and (20) Massalia]. Arredondo et al. find that two asteroids, (7) Iris and (20) Massalia, have a 6-µm feature which is an unambiguous detection of molecular water on their surfaces. (7) Iris and (20) Massalia have estimated water abundances of 374 +/- 202 and 476 +/- 219 µg/g of molecular water on their surfaces. Arredondo et al. note that this abundance of molecular water is consistent with values of molecular water detected on the sunlit surface of the moon (e.g., Honniball et al., 2021, 2022).

Honniball et al. (2021) suggested that the molecular water detected on the sunlit lunar surface is likely created through micrometeorite impacts that have sufficient energy to create H_2O molecules. The molecular water on the lunar surface is likely trapped in impact glass which prevents it from sublimating away. Impacts on the moon generally have more kinetic energy compared to the average relative impact velocities in the asteroid belt. However, Bottke et al. (1994) show there are a wide variety of impact velocities that can occur in the main asteroid belt, for a given object and its unique orbital parameters. Furthermore, the distribution of impact velocities tends to be non-gaussian, for asteroids with high eccentricity and inclination, and has a significant tail of high velocity impacts for many objects. Bottke et al. (1994) also show that asteroids with high inclination and eccentricity can have significantly higher average impact velocities. High inclinations and eccentricities tend to increase the relative encounter speed when asteroid impacts occur, though impacts are generally more infrequent for asteroids on highly inclined or eccentric orbits. While higher velocity impacts in the main belt may be less frequent than impacts on the Moon, it is possible that molecular water detected on (7) Iris and (20) Massalia could be trapped in impact glasses as hypothesized for the Moon. Particularly for (7) Iris which has a high eccentricity (0.23) and a relatively high inclination (5.5°). Higher velocity impacts may explain the signature of water on (7) Iris, with a 3-µm band depth of 5.56 ± 0.97, and the detection may indicate (7) Iris had at least one high velocity impact that produced water molecules.

Several of the asteroids in this study have a high eccentricity [>0.2; (6) Hebe, (18) Melpomene, (82) Alkmene and (7) Iris] and/or a high inclination [>10°; (18) Melpomene, (39) Laetitia, (115) Thyra and (6) Hebe]. (6) Hebe and (18) Melpomene have both a high eccentricity and inclination. (6) Hebe has a non-detection of a 3-µm absorption, indicating it may not have experienced a sufficiently high velocity impact to produce water molecules through impacts as on the moon or enough impacts to deliver exogenic materials. (18) Melpomene's detection of

hydration may indicate the presence of water molecules. Further observations are required to investigate whether molecular water is present on its surface.

The non-detection of molecular water on (11) Parthenope by Arredondo et al. is not surprising given that our spectrum of Parthenope does not have a detectable 3-µm feature. Asteroid (7) Iris, on the other hand, has one of the deepest 3-µm bands in our survey (5.56 +/- 0.97%). Given the Arredondo et al. (2024) results, some of the 3-µm signature observed here is molecular water. However, not all of the 3-µm signatures for the S-complex asteroids presented in this work can be explained by molecular water. (18) Melpomene and (20) Massalia have very similar 3-µm bands with depths of 3.0 +/-1.3% and 3.0 +/- 1.0%, respectively. The fact that Melpomene has a non-detection of molecular water while (20) Massalia has molecular water indicates the complexity of the 3-µm bands for nominally anhydrous main belt S-type asteroids. There does not appear to be a single cause of the signature of hydration but rather multiple factors are at play for the nominally anhydrous asteroids presented here. More 6-µm measurements of molecular water on nominally anhydrous asteroids are needed to further disentangle the contributions of water and OH to the 3-µm signatures on nominally anhydrous asteroids.

5 Implications

5.1 - Mechanism(s) of Hydration: a complex interplay of multiple factors

To determine which mechanism is driving the signature of hydration on these nominally anhydrous objects, we look first at correlations between the 3-µm band depth and physical, orbital, and compositional characteristics as well as observational circumstances. We investigated a wide variety of possibilities, which could point to a number of potential causes for the hydration state we see on these nominally anhydrous bodies.

Physical characteristics like size and albedo could indicate a relationship between hydration and asteroid formation processes, a size dependent ability to retain volatiles, or subsequent geologic evolution of the asteroid. Any relationships with orbital characteristics might point to a dynamical component to the hydration state of S-complex asteroids. Additionally, some of the orbital characteristics like semi-major axis and perihelion/aphelion distance might also indicate a relationship between hydration state and proximity to hydrated asteroids, which are more populous in the middle and outer main belt or close to mean motion resonances. If any relationships exist here, we might consider the hydration effects to be related to exogenic material. We also wanted to consider the possibility that the hydration may be related to seasonality, which motivated the investigation of observational circumstances like instantaneous heliocentric distance and instantaneous theoretical equilibrium temperature. If the signature of hydration for our objects has a relationship with these parameters, it is possible that the hydration is caused by labile water/hydroxyl on the surfaces of these bodies similar to the diurnal cycle of lunar hydration (e.g., Sunshine et al., 2009). Finally, we included a few parameters in this

374 analysis which might point to geometric effects and/or modeling effects which could call into
375 question the validity of the reported 3-µm band depths.
376
377 All of the parameters we linearly regressed with respect to 3-µm band depth, and the resulting
378 relationships and statistics are in **Table 6**. We include the coefficients of the regressions (y =
379 coef1*x + coef2) as well as the root mean squared error, R, student t-value, P value and R^2.
380
381 No physical, orbital, compositional, or circumstantial parameter seemed to have any strong or
382 even moderate correlation with 3-µm band depth.
383
384 Here we consider the correlation coefficient, R, for the regressions. R values occur on a range of
385 [-1, 1] with negative values indicating a negative correlation and positive values indicating a
386 positive correlation. Simply considering the magnitude of the correlations for R values, strong
387 correlations would be 0.7 < |R| < 1, moderate correlations 0.5 < |R| < 0.7, weak correlations 0.3 <
388 |R| < 0.5, and negligible correlations 0.0 < |R| < 0.3. We do not find any moderate or strong
389 correlations between any parameter considered and 3.0-µm band depth. Nominally anhydrous S-
390 complex asteroids in the inner belt do not seem to be related to orbital characteristics, unlike low
391 albedo mid- and outer-main belt asteroids (e.g., Takir and Emery, 2012). Multiple factors are
392 likely at play.
393

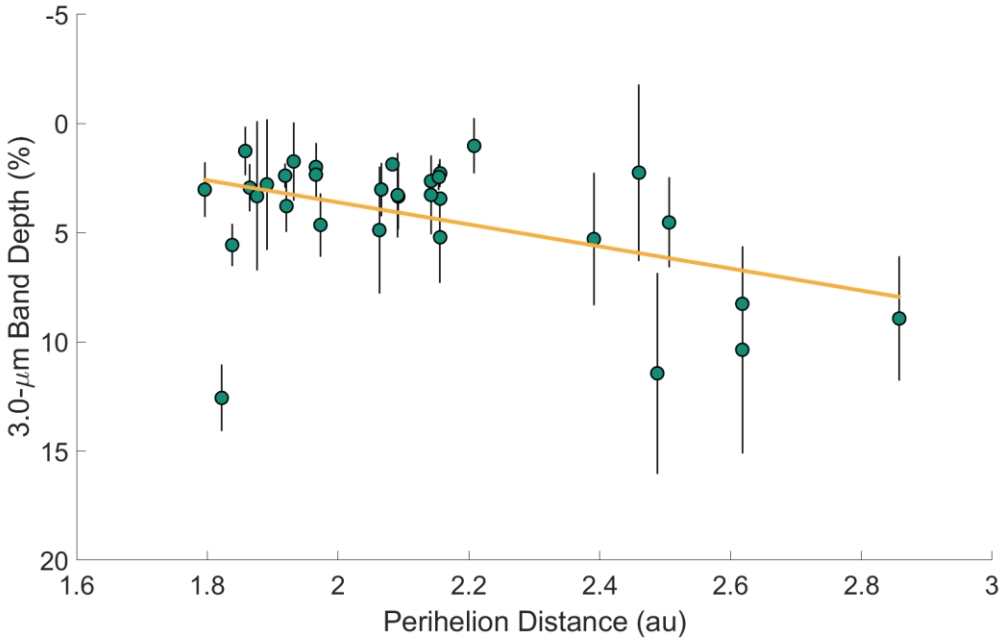

Figure 6: Perihelion distance vs 3.0-µm band depth for all asteroids observed in this work. The relationship between perihelion distance and 3.0-µm band depth for the nominally anhydrous asteroids is weak but it is the best correlation of all parameters that were considered. It seems that there are multiple factors driving the signature of hydration for nominally anhydrous objects. This correlation with perihelion distance could indicate that proximity to hydrated asteroids and exogenic material is one important factor among several hydration mechanisms.

Similarly, there is only a weak correlation with semi-major axis and a negligible correlation with near-infrared slope which suggests that solar wind implantation may not be a primary driving factor of the 3-µm bands observed. Older (redder) surfaces are not more hydrated than younger ones, and those objects closer to the sun (and therefore experiencing more flux of solar wind particles) are also not more hydrated. If solar wind implantation is affecting the 3-µm band on nominally anhydrous main belt asteroids, then this process is complex and not solely dependent on proximity to the Sun nor strictly dependent on size. We hypothesized that orbital characteristics like the aphelion distance might have had some relationship with these nominally anhydrous objects' 3-µm signature. Of the weak correlations found, the parameter that seems to be best correlated with 3.0-µm band depth is perihelion distance (**Figure 6**).

Perihelion distance is correlated with 3.0-µm band depth (R = 0.46) such that with increasing perihelion distance, 3.0-µm band depth also increases. Asteroids with greater perihelion distances spend more time further out in the main asteroid belt. This might indicate that the signature of hydration could be related to proximity to hydrated asteroids in the mid and outer belt and thus the signature of hydration is driven by exogenic delivery of carbonaceous material to these objects. This is similar to the McGraw et al. (2022) result where near-Earth asteroids are found to have a relationship between the signature of hydration and aphelion distance. McGraw et al. (2022) conclude that S-complex near-Earth asteroids may be hydrated due to exogenic sources driven by proximity of the object's orbit to hydrated asteroids in the main belt. Though this correlation is weak, it seems to indicate that solar wind implantation is not a significant contributor to the signature of hydration on nominally anhydrous asteroids.

Still, the relationship between main belt nominally anhydrous asteroids and perihelion distance is a weak correlation and it does not appear that a single factor controls the hydration we report. There is likely a complex interplay between multiple hydration mechanisms here (e.g., exogenic source(s) of hydrated material, target composition, primordially accreted water, dynamical evolution and/or solar wind implantation).

5.2 Comparison to Near-Earth Asteroids

McGraw et al. (2022) report a large study of near-Earth asteroids using near-infrared and 3-µm spectroscopy. In this work they report the spectra of 29 near-Earth S- and Q-type asteroids with detections of hydration on 8 objects. Additionally, they report 3-µm spectral shape groupings that include two varieties of bowls as well as linearly increasing checkmark-like features. The multiple band shapes seem to indicate differences in origin of the 3-µm hydration signature (e.g., checkmark-like shapes more likely to be H implantation; wide-bowls may be exogeneous materials; narrow bowls may either be solar wind or a mix of exogenous materials and solar-wind-implanted H). Proximity to the low-albedo, hydrated mid- and outer main asteroid belt seems to be a significant factor reported in the McGraw et al. work. Near-Earth objects that have large aphelion distances and therefore spend significant time in the asteroid belt seem to have 3-

μm. Composition, additionally, seems to be a significant factor. Near-Earth asteroids with V-type taxonomic classification do not have detectable 3.0-μm bands.

Comparing the eight near-Earth asteroids that have a 3.0-μm feature, our main belt asteroid data set is broadly similar to the near-Earth asteroids. The near-Earth S- and Q-types tend to have band depths between 2.5-5%. Most of the main belt S-complex asteroids have similar band depths. It appears that our dataset is mostly consistent with the results of McGraw et al. (2022) in that proximity to the more hydrated mid- and outer belt seems to be one significant factor in a complex relationship with the signature of hydration. This, however, is where the similarities in our datasets end.

McGraw et al. (2022) report 3.0-μm band shape groupings (e.g., wide/narrow linear, wide/narrow bowls). The vast majority of the large main belt S-complex asteroids reported here have essentially flat spectra between 2.9 – 3.4-μm. This is to say that the reflectance between 2.9-3.4-μm is roughly the same reflectance value for all the large main belt S-complex asteroids presented here. There do not appear to be any shape groupings or variations in the 3-μm band shape, particularly for the large asteroids. We may see some similarities between (208) Lacrimosa and Type 1 (wide linear) checkmark shape, (808) Merxia and Type 2 (narrow linear) checkmark shape, and (277) Elvira, (352) Gisela and (462) Eriphyla and Type 3 (wide bowl) shape. Yet, 85% of the objects reported here are flat and even those with some similarities may be caused by some lingering unameliorated telluric contamination. There may be a number of reasons for the lack of similarities between these two datasets.

The near-Earth asteroids reported in McGraw et al. (2022) are generally significantly smaller than the objects observed in the main belt. We report spectra for only two objects with diameters ~10 km or less, whereas McGraw et al. present spectra for 18 objects of 10 km diameter or less (most of these are ~5 km or less in size; we have no objects below 5 km diameter). We report spectra for 6 asteroids between 10-40 km in diameter. This difference in our samples is driven by the underlying characteristics of the two populations. The near-Earth asteroid population tends to be small, smaller than ~40 km in size while the main belt has a power law distribution of asteroids of 1000 km or less. This difference in sizes and the greater distance to the asteroid belt result in an observational bias between the asteroid population investigated in this and work that of McGraw et al. (2022). Beyond their orbital characteristics, the asteroids reported in this work are typically at least one order of magnitude larger than the objects reported in McGraw et al. (2022).

It is intriguing that some of the main belt asteroids in this work with <40 km diameter do seem to have some spectral type similarity with McGraw et al. Type 3 band morphology. The near-Earth asteroid (1036) Ganymed has a diameter of ~40 km also and exhibits Type 3 spectral characteristics. Based on recent missions to small near-Earth objects (Yoshikawa et al., 2006; Ho et al., 2021; DellaGiustina et al., 2019) asteroids with very small diameters have significantly more boulders and large-grained regoliths. Perhaps larger grains interact differently with the

solar wind and/or retain OH/H_2O differently than larger asteroids with finer grained regoliths. More observations of Main Belt asteroids between 10-40 km would be necessary to investigate this hypothesis. Additionally, laboratory studies of the effect of grain size on solar wind implantation of OH could also further our understanding of the systematic differences between large and small asteroids.

5.3 Comparison to Vesta

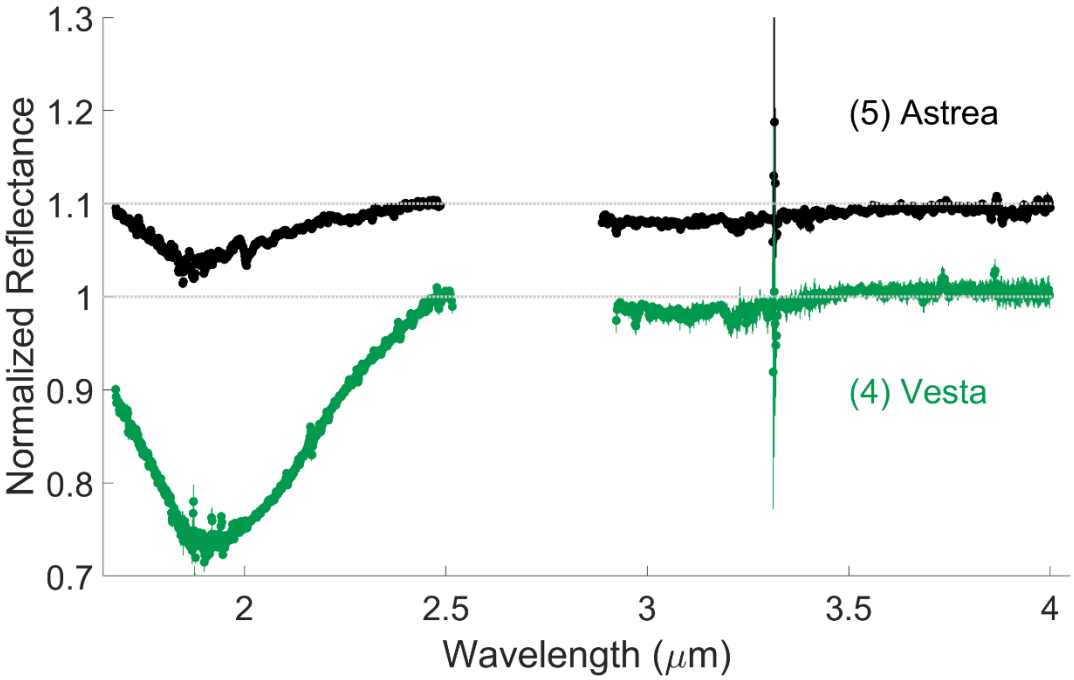

Figure 7: Comparison of an example S-complex asteroid [(5) Astrea] and (4) Vesta. Vesta was observed by the IRTF and this spectrum was published in McGraw et al., 2022. Vesta has a similar 3-µm band to the majority of the S-complex asteroids presented in this work. Vesta has a much deeper 2-µm band due to Vesta's differentiated mineralogy. The leading explaination for the signature of hydration on Vesta is exogenic material. The similarity between Vesta and the S-complex asteroids supports the hypothesis that the 3-µm bands on S-complex asteroids is driven by exogenic material.

McGraw et al. (2022) report a 3.0-µm detection for (4) Vesta which is consistent with previous observations made using ground-based telescopes (Hasegawa et al., 2003) and global detections from the Dawn Mission (De Sanctis et al., 2012). Vesta's 3.0-µm band is reported to be 2.4±0.9% which is also consistent with many of the S-complex asteroids reported in this work. **Figure 7** shows a comparison to an IRTF spectrum of Vesta from McGraw et al., (2022) and an S-type [(5) Astrea]. The spectrum reported in McGraw et al. (2022) appears to have a flat shape, like the S-complex asteroids presented here. The consistency across Vesta and the nominally anhydrous main belt S-complex asteroids seems to support the hypothesis of exogenic material as a significant, though not sole, factor in the signature of hydration for large main belt S-complex asteroids.

Vesta was known to have a signature of hydration prior to the arrival of the Dawn spacecraft in 2011 (e.g., Hasegawa et al., 2003) and that this signature was detected all over the surface (e.g., Rivkin et al., 2006). The Dawn Mission globally mapped Vesta confirming this detection (e.g., De Sanctis et al., 2012). Researchers found that the 3-μm band was associated with dark material on Vesta's surface (e.g., McCord et al., 2012; Reddy et al., 2012).

The presence of dark materials on Vesta's surface varies spatially, with detections in crater rims, walls and ejecta blankets as well as some exposures in Vesta's mid-latitude hills (e.g., Reddy et al., 2012; McCord et al., 2012). Reddy et al. (2012) show that one large crater in particular, Venenia, has a high concentration of dark material in its crater walls. While other materials on Vesta can be dark (e.g., impact melts/shock-darkened materials, pyroclastic deposits, fine-grained eucrites with quenched textures, opaque materials such as metal and tochilinite), the association of 3-μm signatures with the vestan dark material indicated that the composition is most similar to aqueously altered carbonaceous meteorites. These carbonaceous materials are inconsistent with any potential endogenic source on Vesta, so it was concluded that they were delivered from exogenic sources. This conclusion was further supported by the presence of unshocked carbonaceous clasts in HED meteorites (e.g., Rubin and Bottke, 2009). Carbonaceous-like clasts, Rubin and Bottke (2009) report, are the most abundant foreign clasts in HEDs.

Vesta, as one of the most studied asteroids, is an important comparison point for the S-complex asteroids in this study. Given that there are several potential scenarios for the delivery of exogenic hydrated materials to Vesta, we now consider if similar delivery scenarios are possible for S-complex asteroids. First, it should be noted that carbonaceous chondrite clasts are also the most abundant foreign clasts found in H ordinary chondrites (Rubin and Bottke, 2009). Given the potential link between some S-complex asteroids and ordinary chondrites, this observation serves as an independent confirmation of exogenic material.

If exogenic material is delivered by impacts, as hypothesized for Vesta (e.g., McCord et al., 2012; Reddy et al., 2012), there are several key factors involved in the estimate of its delivery. Impact velocity and the probability of impacts are the first key factors. According to Bottke et al. (1994), the impact probability and the distribution of relative impact velocities are unique to each asteroid, depending on its size and orbital parameters. The distribution of relative impact velocities for asteroids in the main belt with relatively small inclination and eccentricity tends to be non-gaussian. Impacts may occur at velocities higher or lower than the average impact velocity in the asteroid belt. In the case of Vesta, ~6% of impacts would have been slow enough to allow a 10-30 km sized object impact and retain a significant proportion of the projectile material (e.g., Reddy et al., 2012). Asteroids on more inclined or eccentric orbits tend to have higher relative impact velocities compared to the average impact velocity of the main belt. The impact probability for asteroids on these orbits is lower because they do not cross as many objects as co-planar orbits. However, these higher impact velocities may be sufficiently energetic

to form molecular water, similar to the process for lunar molecular water production (e.g., Honniball et al., 2021).

In the event that impacts occur with the right speed and angle, the amount of the projectile mass retained by the asteroid is the next critical factor. The amount of the impactor body that is retained on an asteroid is dependent on the target body's size, the relative impact speed and impact angle. According to hydrodynamic simulations and impact scaling laws presented in Svetsov (2011), slower impact velocities allow more impactor mass to be retained. However, for a given impact speed, smaller asteroids retain less impactor mass and significant target mass is lost in comparison to impacts on larger objects. Still, even for objects with sizes of ~50 – 200 km diameter at moderate (5 km/s) impact speeds and low (1.25 km/s) impact speeds, the retained impactor mass can range from 35-75%. These scaling laws are supported by laboratory studies that find significant survival of impactor mass and minimal impactor melting (Avdellidou et al., 2016).

While the S-complex asteroids studied in this work are smaller than Vesta, it may be possible that these bodies experienced exogenic material delivering impacts with sufficient retention that this exogenic material would be detectable today. The peculiarities that affect impact probability, speed and retention are unique to each object and complex. The complexity involving size and orbital parameters may explain why we do not see any correlations of 3-µm band depth with other parameters. A detailed investigation of the probabilities of each asteroid in the style of O'Brien et al. (2011), McCord et al. (2012) and Reddy et al. (2012) is beyond the scope of this work. However, those investigations would likely provide insights into the signature of hydration detected on the asteroids presented here.

5.4 – Investigating the H ordinary chondrite-like asteroids

One potential way to begin to understand how multiple factors may be affecting the signature of hydration is to consider asteroids that have a strong compositional similarity. In general, there are two ways to investigate asteroids with a strong compositional similarity: collisional families or asteroids with strongly similar spectral properties. We do not have a sufficient number of asteroids within families to investigate how 3-µm band depth may vary. Still, we acknowledge that this could be a fruitful investigation in the future. Aside from investigating families, there is another method for exploring asteroids with compositional similarity.

As described in **Appendix 1,** we see that a large subset of this sample of asteroids is consistent with ordinary chondrite-like mineralogy, plotting in the ordinary chondrite boot region of the Gaffey plot (**Figure 3**). Further analysis described in **Appendix 2** identifies asteroids that are compositionally consistent with H ordinary chondrites.

The H ordinary chondrite-like asteroids (**Table 7**) are the most numerous subgroup of objects in our study, representing ~30% of the objects/observations reported here. Additionally, there is some evidence that the H and L ordinary chondrites may have come from the same asteroid (Keil et al., 1994). We include the single L-like asteroid in these analyses as well. We now consider only these asteroids to investigate correlations between the parameters described above and this subset.

We proceed with these correlations with an abundance of caution. This is a very small number of objects and any relationships that are found must be absorbed with a grain of metaphorical salt. More observations of nominally anhydrous asteroids, especially compositionally linked asteroids, are needed to confirm any relationships we find here.

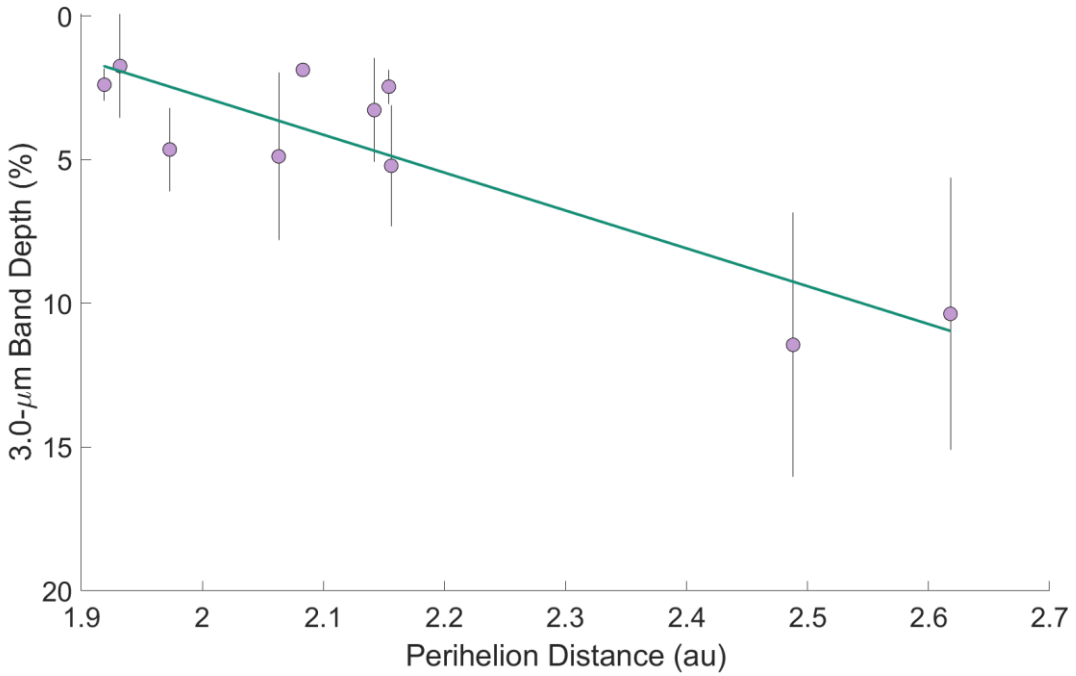

Figure 8: H ordinary chondrite like asteroids' perihelion distance vs. 3.0-µm band depth. This (with eccentricity) is the strongest correlation for the H ordinary chondrite like asteroids and their 3.0-µm band depth. This correlation indicates that the larger the perihelion distance, the deeper the 3.0-µm band. This may indicate that proximity to the lower albedo, more hydrated mid and outer belt objects is a primary driver of the signature of hydration observed.

Considering only the compositionally linked ordinary chondrite-like asteroids, we find three strong correlations with 3.0-µm band depth: eccentricity (R = 0.88, P = 0.00071), perihelion distance (R = 0.88, P= 0.0076) and Band II center (R = 0.72, P = 0.019).

The strong correlation between the H chondrite-like asteroids and perihelion distance (**Figure 8**) could hint that hydration is related to exogenic material. Similar to the conclusions of McGraw et al. (2022), the asteroids that have greater perihelion distances spend more of their time closer to the lower albedo and generally more hydrated mid- and outer-main asteroid belt. The proximity

to those objects could increase the likelihood of impacts of hydrated material. One contributing factor to the signature of hydration on nominally anhydrous asteroids could be exogenic material.

The R values of the eccentricity (**Figure 9**) and perihelion distance (**Figure 8**) correlations are nearly identical. This similarity may be driven by this underlying bias in the objects we observed. One potential cause of this underlying bias is that the inner main belt experienced a late excitation event that shaped the eccentricity distribution (e.g., Malhorta and Wang 2016). The asteroids in our dataset with the greatest perihelion distance have the lowest eccentricities.

Band II is caused by the abundance and composition of pyroxene in S-complex asteroids and ordinary chondrites. The Band II center position's correlation with 3-µm band depth covers a very small change in Band II position. Because these objects are compositionally linked, this band has virtually the same position for all the objects in this subset. The difference in position is ~0.05-µm. This is well within the error of the measurement and so this correlation is likely spurious.

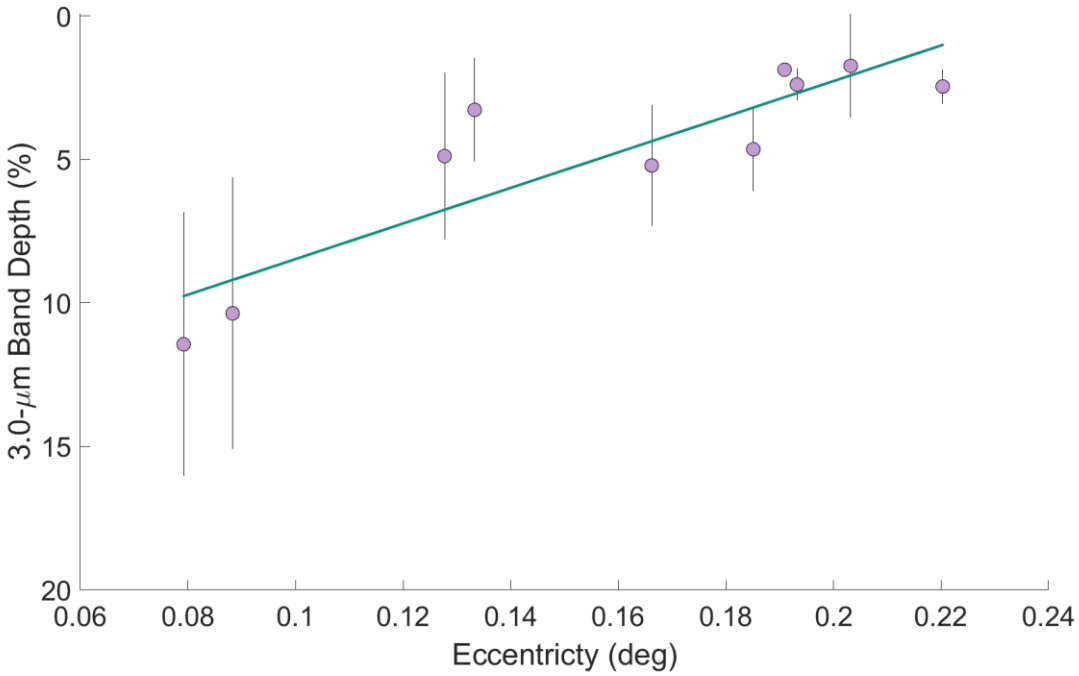

Figure 9: 3.0-µm band depth vs eccentricity for H ordinary chondrite like asteroids. For the objects in this study that are similar to H ordinary chondrites, eccentricity has the strongest relationship with 3.0-µm band depth. For asteroids with lower eccentricities the band depth is deepest; for those with higher eccentricities, the band depth is shallower. Higher orbital eccentricities indicate dynamical excitation. Shallower band depths may indicate that the dynamical evolution is playing a part in band depths. Alternatively, asteroids with less dynamical excitation are more likely to be on nearly circular, co-planar orbits and may, therefore, likely have a greater flux of exogenic material compared to those with orbits that cause the asteroid to be out of the plane for much of its orbit.

The relationship between eccentricity and band depth is a strong negative correlation (**Figure 9**): the asteroids with the deepest 3-µm bands have the lowest eccentricities while asteroids with the shallowest 3-µm bands have the highest eccentricities. Bottke et al. (1994) show that asteroids with high inclination and eccentricity tend to have higher relative impact speeds. Impacts are less likely to occur for asteroids with higher eccentricity and/or inclination. Moreover, these impacts would retain less impactor mass and erode more target mass when they do occur (e.g., Svetsov, 2011). The correlation with eccentricity may indicate that asteroids with more circular, co-planar orbits are more likely to experience lower speed impacts thus allowing them to retain more exogenic material compared to those asteroids on more eccentric orbits.

6 – Conclusions

We have presented a large 3-µm survey of nominally anhydrous S-complex asteroids in the main asteroid belt. Our primary result is that 23 of the 29 objects we observe show the signature of hydration through the telltale 3-µm absorption. The objects in the study have variable amounts of hydration from very little (~1% band depth) to significant (>10% band depth) which is comparable with some of the hydrated low-albedo main belt objects (Takir and Emery 2012), though the shapes of the 3-µm band differ from low-albedo asteroids and S- and Q-type near-Earth asteroids (McGraw et al., 2022). Overall, it appears that hydration of nominally anhydrous asteroids is controlled by multiple factors; there is no single, straightforward explanation for the signature of hydration detected on nominally anhydrous asteroids in the main belt. Potentially, the signature hydration could be related to the perihelion distance of the asteroid. This correlation, however, is weak. This weak correlation suggests that solar wind implantation is perhaps not a significant source, as band depth increases with increasing perihelion. It follows that exogenic delivery of hydrated material may, however, be a significant source. When we investigate asteroids that appear to be consistent with H ordinary chondrite lithologies, which likely share compositional characteristics and parent body evolution, we find that eccentricity and perihelion distance are strongly correlated with 3-µm band depth. This could indicate an exogenic source for the signature of hydration.

It seems likely that exogenic material is a significant driving factor of the signature of hydration for nominally anhydrous asteroids given the weak correlation with perihelion distance for the whole sample and the strong correlation with eccentricity for the H ordinary chondrite-like asteroids. Asteroids with lower eccentricity are more likely to experience low speed impacts which would enable exogenic material to be retained. Asteroids on more eccentric orbits tend to experience higher speed though less frequent impacts (e.g., Bottke et al., 1994). Exogenic delivery is still only one contributing factor to the signature of hydration observed. More observations are necessary to untangle what is driving the 3-µm signature.

Acknowledgements

This work was funded on a Near-Earth Object Observations Program grant numbers NNX16AE91G and 80NSSC20K0291

The data for this paper was collected at the Infrared Telescope Facility, which is operated by the University of Hawaii under contract 80HQTR19D0030 with the National Aeronautics and Space Administration.

Principle component analysis results presented in this work were determined, in whole or in part, using a Bus-DeMeo Taxonomy Classification Web tool by Stephen M. Slivan, developed at MIT with the support of National Science Foundation Grant 0506716 and NASA Grant NAG5-12355.

Division of labor amongst coauthors: Observations: Thomas 17 runs (57%), McGraw 7.5 runs (25%), Emery 4.5 runs (15%), Richard Cartwright 1 run (3%). Data reduction: University of Tennessee (Knoxville) undergraduate supervised by McGraw and Emery 3 observations, McAdam 36 observations with significant support/troubleshooting from McGraw, Rivkin, Thomas and Emery. Analysis: all performed by McAdam with significant support from Thomas. Additional Data: reduced LXD observations of nominally anhydrous asteroids by Rivkin.

We thank Brittany Harvison and Juan Sanchez for crosschecking our band parameter analysis. We also thank Richard Cartwright for assisting in the data collection.

References:

Alexander, C.D., Barber, D.J. and Hutchison, R., 1989. The microstructure of Semarkona and Bishunpur. Geochimica et Cosmochimica Acta, 53(11), pp.3045-3057.

Altwegg, K., Balsiger, H., Bar-Nun, A., Berthelier, J.J., Bieler, A., Bochsler, P., Briois, C., Calmonte, U., Combi, M., De Keyser, J. and Eberhardt, P., 2015. 67P/Churyumov-Gerasimenko, a Jupiter family comet with a high D/H ratio. Science, 347(6220), p.1261952.

Arredondo, A., McAdam, M., Honniball, C. I., Becker, T. M., Emery, J. P., Rivkin, A. S., Takir, D., Thomas, C. A., Detection of molecular H2O on nominally anhydrous asteroids. 2024. Planetary Science Journal, 5(2), p 37.

Avdellidou, C., Price, M.C., Delbo, M., Ioannidis, P. and Cole, M.J., 2016. Survival of the impactor during hypervelocity collisions–I. An analogue for low porosity targets. Monthly Notices of the Royal Astronomical Society, 456(3), pp.2957-2965.

Baliunas, S., Donahue, R., Rampino, M.R., Gaffey, M.J., Shelton, J.C. and Mohanty, S., 2003. Multispectral analysis of Asteroid 3 Juno taken with the 100-inch telescope at Mount Wilson Observatory. Icarus, 163(1), pp.135-141.

Batrakov, Y.V., Prokofjeva-Mikhajlovskaya, V.V. and Karachkina, L.G., 2010. The small libration of the satellite in the system of the asteroid 39 Laetitia. ББК 22.655 340, p.95.

Bell, J.F., Davis, D.R., Hartmann, W.K. and Gaffey, M.J., 1989. Asteroids: The big picture. Asteroids II (eds. R.P. Binzel, T. Gehrels, M. S. Matthews), University of Arizona press., pp.921-945.

BENNETT III, M.E. and McSween Jr, H.Y., 1996. Revised model calculations for the thermal histories of ordinary chondrite parent bodies. Meteoritics & Planetary Science, 31(6), pp.783-792.

Bobrovnikoff, NT, 1929. The spectra of minor planets. Lick Observatory Bulletin , 14 , pp.18-27.

Bockelée-Morvan, D., Gautier, D., Lis, D.C., Young, K., Keene, J., Phillips, T., Owen, T., Crovisier, J., Goldsmith, P.F., Bergin, E.A. and Despois, D., 1998. Deuterated water in comet C/1996 B2 (Hyakutake) and its implications for the origin of comets. Icarus, 133(1), pp.147-162.

Bottke Jr, W.F., Nolan, M.C., Greenberg, R. and Kolvoord, R.A., 1994. Velocity distributions among colliding asteroids. Icarus, 107(2), pp.255-268.

Bowell, E., Chapman, C.R., Gradie, J.C., Morrison, D. and Zellner, B., 1978. Taxonomy of asteroids. Icarus, 35(3), pp.313-335.

Brearley, A.J., 2006. The action of water. Meteorites and the early solar system II, 943, pp.587-624.

Benna, M., Hurley, D.M., Stubbs, T.J., Mahaffy, P.R. and Elphic, R.C., 2019. Lunar soil hydration constrained by exospheric water liberated by meteoroid impacts. Nature Geoscience, 12(5), pp.333-338.

Broglia, P., Manara, A. and Farinella, P., 1994. Polarimetric observations of (6) Hebe. Icarus, 109(1), pp.204-209.

Brownlee, D., 2014. The Stardust mission: analyzing samples from the edge of the solar system. Annual Review of Earth and Planetary Sciences, 42, pp.179-205.

Burbine, T.H. and Binzel, R.P., 2002. Small main-belt asteroid spectroscopic survey in the near-infrared. *Icarus*, *159*(2), pp.468-499.

Busarev, V.V., 2002. Hydrated silicates on M-, S-, and E-type asteroids as possible traces of collisions with bodies from the Jupiter growth zone. Solar System Research, 36(1), pp.35-42.

735 Campins, H., Hargrove, K., Pinilla-Alonso, N., Howell, E.S., Kelley, M.S., Licandro, J., Mothé-
736 Diniz, T., Fernández, Y. and Ziffer, J., 2010. Water ice and organics on the surface of the
737 asteroid 24 Themis. Nature, 464(7293), pp.1320-1321.
738
739 Campins, H., Hargrove, K., Pinilla-Alonso, N., Howell, E.S., Kelley, M.S., Licandro, J., Mothé-
740 Diniz, T., Fernández, Y. and Ziffer, J., 2010. Water ice and organics on the surface of the
741 asteroid 24 Themis. Nature, 464(7293), pp.1320-1321.
742
743 Canup, R.M., 2004. Dynamics of lunar formation. Annual review of astronomy and astrophysics,
744 42(1), pp.441-475.
745
746 Carruba, V., Nesvorný, D., Aljbaae, S. and Huaman, M.E., 2015. Dynamical evolution of the
747 Cybele asteroids. Monthly Notices of the Royal Astronomical Society, 451(1), pp.244-256.
748 Chapman, C.R. and Salisbury, J.W., 1973. Comparisons of meteorite and asteroid spectral
749 reflectivities. Icarus, 19(4), pp.507-522.
750
751 Chapman, C.R., Morrison, D. and Zellner, B., 1975. Surface properties of asteroids: A synthesis
752 of polarimetry, radiometry, and spectrophotometry. Icarus, 25(1), pp.104-130.
753
754 Clark, R.N., 2009. Detection of adsorbed water and hydroxyl on the Moon. Science, 326(5952),
755 pp.562-564.
756
757 Cloutis, E.A., Gaffey, M.J., Smith, D.G. and Lambert, R.S.J., 1990. Metal silicate mixtures:
758 Spectral properties and applications to asteroid taxonomy. Journal of Geophysical Research:
759 Solid Earth, 95(B6), pp.8323-8338.
760
761 Clutz, F.H., 1899. Determination of the Orbit of Planetoid 115 Thyra. TP Nichols.
762 Cushing, M.C., Vacca, W.D. and Rayner, J.T., 2004. Spextool: A spectral extraction package for
763 SpeX, a 0.8–5.5 micron cross-dispersed spectrograph. Publications of the Astronomical Society
764 of the Pacific, 116(818), p.362.
765
766 Davison, T.M., Collins, G.S. and Ciesla, F.J., 2008, March. Hydrocode Modelling of Melt
767 Production in Planetesimal Collisions. In 39th Annual Lunar and Planetary Science Conference
768 (No. 1391).
769
770 De Sanctis, M.C., Combe, J.P., Ammannito, E., Palomba, E., Longobardo, A., McCord, T.B.,
771 Marchi, S., Capaccioni, F., Capria, M.T., Mittlefehldt, D.W. and Pieters, C.M., 2012. Detection
772 of widespread hydrated materials on Vesta by the VIR imaging spectrometer on board the Dawn
773 mission. The Astrophysical Journal Letters, 758(2), p.L36.
774
775 De Sanctis, M.C., Mitri, G., Castillo-Rogez, J., House, C.H., Marchi, S., Raymond, C.A. and
776 Sekine, Y., 2020. Relict ocean worlds: Ceres. Space Science Reviews, 216, pp.1-33.
777

Degewij, J., Tedesco, E.F. and Zellner, B., 1979. Albedo and color contrasts on asteroid surfaces. Icarus, 40(3), pp.364-374.

Deienno R., Izidoro A., Nesvorný D., Bottke W. F., Size-Frequency Distribution of S-complex Implanted Asteroids. Asteroids Comets Meteors Conference, abstract 2549.

DellaGiustina, D.N., Emery, J.P., Golish, D.R., Rozitis, B., Bennett, C.A., Burke, K.N., Ballouz, R.L., Becker, K.J., Christensen, P.R., Drouet d'Aubigny, C.Y. and Hamilton, V.E., 2019. Properties of rubble-pile asteroid (101955) Bennu from OSIRIS-REx imaging and thermal analysis. Nature Astronomy, 3(4), pp.341-351.

DeMeo, F.E., Binzel, R.P., Slivan, S.M., and Bus, S.J., 2009. An Extension of the Bus Asteroid Taxonomy into the Near-Infrared. Icarus 202, pp. 160-180.

Dobrică, E., Engrand, C., Duprat, J., Gounelle, M., Leroux, H., Quirico, E. and Rouzaud, J.N., 2009. Connection between micrometeorites and Wild 2 particles: From Antarctic snow to cometary ices. Meteoritics & Planetary Science, 44(10), pp.1643-1661.

Dodd, R.T., 1981. Meteorites: A petrologic-chemical synthesis. CUP Archive.

Donahue, T.M. and Hodges Jr, R.R., 1993. Venus methane and water. Geophysical research letters, 20(7), pp.591-594.

Dunham, D. W. and Herald, D., Asteroid Occultations V4.0. EAR-A-3-RDR-OCCULTATIONS-V4.0. NASA Planetary Data System, 2006.

Dunn, T.L., McCoy, T.J., Sunshine, J.M. and McSween Jr, H.Y., 2010. A coordinated spectral, mineralogical, and compositional study of ordinary chondrites. Icarus, 208(2), pp.789-797.

Dykhuis, M.J., Molnar, L.A., Gates, C.J., Gonzales, J.A., Huffman, J.J., Maat, A.R., Maat, S.L., Marks, M.I., Massey-Plantinga, A.R., McReynolds, N.D. and Schut, J.A., 2016. Efficient spin sense determination of Flora-region asteroids via the epoch method. Icarus, 267, pp.174-203.

Eaton, N., Green, S.F., McCheyne, R.S., Meadows, A.J. and Veeder, G.J., 1983. Observations of asteroids in the 3-to 4-μm region. Icarus, 55(2), pp.245-249.

Farinella, P., Froeschlé, C. and Gonczi, R., 1993. Meteorites from the asteroid 6 Hebe. Celestial Mechanics and Dynamical Astronomy, 56(1), pp.287-305.

Feierberg, M.A., Witteborn, F.C. and Lebofsky, L.A., 1983. Detection of silicate emission features in the 8-to 13-μm spectra of main belt asteroids. Icarus, 56(3), pp.393-397.

Ferguson, J., 1856. Observations of (11) Parthenope,(16) Psyche (36) Atalanta,(37) Fides,(38) Leda, the thirty-ninth asteroid, and comet 1855, III. The Astronomical Journal, 4, pp.156-159.

Florczak, M., Barucci, M.A., Doressoundiram, A., Lazzaro, D., Angeli, C.A. and Dotto, E., 1998. A visible spectroscopic survey of the Flora clan. Icarus, 133(2), pp.233-246.

Fu, R.R. and Elkins-Tanton, L.T., 2014. The fate of magmas in planetesimals and the retention of primitive chondritic crusts. Earth and Planetary Science Letters, 390, pp.128-137.

Gaffey, M.J. and Fieber-Beyer, S.K., 2019, March. Is the (20) Massalia Family the source of the L-Chondrites. In 50th Lunar and Planetary Science Conference.

Gaffey, M.J. and Gilbert, S.L., 1998. Asteroid 6 Hebe: The probable parent body of the H-type ordinary chondrites and the IIE iron meteorites. Meteoritics & Planetary Science, 33(6), pp.1281-1295.

Gaffey, M.J., Bell, J.F., Brown, R.H., Burbine, T.H., Piatek, J.L., Reed, K.L. and Chaky, D.A., 1993. Mineralogical variations within the S-type asteroid class. Icarus, 106(2), pp.573-602.

Ghosh, A., Weidenschilling, S.J. and McSWEEN Jr, H.Y., 2003. Importance of the accretion process in asteroid thermal evolution: 6 Hebe as an example. Meteoritics & Planetary Science, 38(5), pp.711-724.

Gradie, J. and Tedesco, E., 1982. Compositional structure of the asteroid belt. Science, 216(4553), pp.1405-1407.

Granahan, J.C., 2011. Spatially resolved spectral observations of Asteroid 951 Gaspra. Icarus, 213(1), pp.265-272.

Granahan, J.C., Fanale, F.P., Robinson, M.S., Carlson, R.W., Kamp, L.W., Klaasen, K.P., Weissman, P.R., Belton, M., Cook, D., Edwards, K. and McEwen, A.S., 1994, March. A Galileo multi-instrument spectral analysis of 951 Gaspra. In Abstracts of the 25th Lunar and Planetary Science Conference, held in Houston, TX, 14-18 March 1994., p. 453 (Vol. 25, p. 453).

Grimm, R.E. and McSween Jr, H.Y., 1993. Heliocentric zoning of the asteroid belt by aluminum-26 heating. Science, 259(5095), pp.653-655.

Groeneveld, I. and Kuiper, G.P., 1954. Photometric studies of asteroids. I. The Astrophysical Journal, 120, p.200.

Hanuš, J., Marsset, M., Vernazza, P., Viikinkoski, M., Drouard, A., Brož, M., Carry, B., Fetick, R., Marchis, F., Jorda, L. and Fusco, T., 2019. The shape of (7) Iris as evidence of an ancient large impact?. Astronomy & Astrophysics, 624, p.A121.

Harris, A.W., 1998. A thermal model for near-Earth asteroids. Icarus, 131(2), pp.291-301.

Harwood, M., 1924. Variations in the Light of Asteroids. Harvard College Observatory Circular, 269, pp.1-15.

Hasegawa, S., Murakawa, K., Ishiguro, M., Nonaka, H., Takato, N., Davis, C.J., Ueno, M. and Hiroi, T., 2003. Evidence of hydrated and/or hydroxylated minerals on the surface of asteroid 4 Vesta. Geophysical Research Letters, 30(21).

Hestroffer, D., Tanga, P., Berthier, J., Cellino, A., Lattanti, M., Di Martino, M. and Zappala, V., 2002. HST/FGS interferometric observations of asteroids. Memorie della Società astronomica italiana, 73, p.674.

Hibbitts, C.A., Grieves, G.A., Poston, M.J., Dyar, M.D., Alexandrov, A.B., Johnson, M.A. and Orlando, T.M., 2011. Thermal stability of water and hydroxyl on the surface of the Moon from temperature-programmed desorption measurements of lunar analog materials. Icarus, 213(1), pp.64-72.

Ho, T.M., Jaumann, R., Bibring, J.P., Grott, M., Glaßmeier, K.H., Moussi, A., Krause, C., Auster, U., Baturkin, V., Biele, J. and Cordero, F., 2021. The MASCOT lander aboard Hayabusa2: the in-situ exploration of NEA (162173) Ryugu. Planetary and Space Science, 200, p.105200.

Honniball, C.I., Lucey, P.G., Arredondo, A., Reach, W.T. and Malaret, E.R., 2022. Regional Map of Molecular Water at High Southern Latitudes on the Moon Using 6 μm Data From the Stratospheric Observatory for Infrared Astronomy. Geophysical Research Letters, 49(9), p.e2022GL097786.

Honniball, C.I., Lucey, P.G., Li, S., Shenoy, S., Orlando, T.M., Hibbitts, C.A., Hurley, D.M. and Farrell, W.M., 2021. Molecular water detected on the sunlit Moon by SOFIA. Nature Astronomy, 5(2), pp.121-127.

Hyden, J., Thomas, C., Harvison, B., Lucas, M., Trilling, D., Moskovitz, N. and Lim, L., 2020, January. Spectral Analysis of the Massalia Asteroid Family. In American Astronomical Society Meeting Abstracts# 235 (Vol. 235, pp. 277-07).

Izidoro A., Deienno R., Dasgupta R., Isella A., 2023. The effect of the solar system early dynamical instability on the asteroid belt implantation. Asteroids Comets Meteors Conference, abstract 2544.

Jarosewich, E., 1990. Chemical analyses of meteorites: A compilation of stony and iron meteorite analyses. Meteoritics, 25(4), pp.323-337.

Jiang, H., Ji, J. and Yu, L., 2020. Determination of Size, Albedo, and Thermal Inertia of 10 Vesta Family Asteroids with WISE/NEOWISE Observations. The Astronomical Journal, 159(6), p.264.

Johansen et al., 2015 (check Malborta/Want 2016 paper) look it up in Asteroids IV
Johansen, A., Jacquet, E., Cuzzi, J.N., Morbidelli, A. and Gounelle, M., 2015. New paradigms for asteroid formation. Asteroids IV, 47, pp.1-492.

Jones, T.D., Lebofsky, L.A., Lewis, J.S. and Marley, M.S., 1990. The composition and origin of the C, P, and D asteroids: Water as a tracer of thermal evolution in the outer belt. Icarus, 88(1), pp.172-192.

Keil, K., Haack, H. and Scott, E.R.D., 1994. Catastrophic fragmentation of asteroids: Evidence from meteorites. Planetary and Space Science, 42(12), pp.1109-1122.Klima et al., 2011
Kelley, M.S. and Gaffey, M.J., 2000. 9 Metis and 113 Amalthea: A genetic asteroid pair. Icarus, 144(1), pp.27-38.

Landsman, Z.A., Campins, H., Pinilla-Alonso, N., Hanuš, J. and Lorenzi, V., 2015. A new investigation of hydration in the M-type asteroids. Icarus, 252, pp.186-198.

Lawrence, D.J., Feldman, W.C., Goldsten, J.O., Maurice, S., Peplowski, P.N., Anderson, B.J., Bazell, D., McNutt Jr, R.L., Nittler, L.R., Prettyman, T.H. and Rodgers, D.J., 2013. Evidence for water ice near Mercury's north pole from MESSENGER Neutron Spectrometer measurements. Science, 339(6117), pp.292-296.

Lehtinen, K., Bach, U., Muinonen, K., Poutanen, M. and Petrov, L., 2016. Asteroid sizing by radiogalaxy occultation at 5 GHz. The Astrophysical Journal Letters, 822(2), p.L21.

Levison, Harold F., Katherine A. Kretke, and Martin J. Duncan. "Growing the gas-giant planets by the gradual accumulation of pebbles." Nature 524, no. 7565 (2015): 322-324.

Love, S.G. and Allton, J.H., 2006. Micrometeoroid impact crater statistics at the boundary of Earth's gravitational sphere of influence. Icarus, 184(2), pp.302-307.

Love, S.G. and Brownlee, D.E., 1993. A direct measurement of the terrestrial mass accretion rate of cosmic dust. Science, 262(5133), pp.550-553.

Lucas, M.P., Emery, J.P., Hiroi, T. and McSween, H.Y., 2019. Spectral properties and mineral compositions of acapulcoite–lodranite clan meteorites: Establishing S-type asteroid–meteorite connections. Meteoritics & Planetary Science, 54(1), pp.157-180.

Lupishko, D.F. and Velichko, F.P., 1987. Sense of rotation of asteroids 21, 63, 216 and 349. Kinematika i Fizika Nebesnykh Tel, 3, pp.57-65.

Malhotra, R. and Wang, X., 2017. Eccentricity distribution in the main asteroid belt. Monthly Notices of the Royal Astronomical Society, 465(4), pp.4381-4389.

Marchis, F., Kaasalainen, M., Hom, E.F.Y., Berthier, J., Enriquez, J., Hestroffer, D., Le Mignant, D. and De Pater, I., 2006. Shape, size and multiplicity of main-belt asteroids: I. Keck Adaptive Optics survey. Icarus, 185(1), pp.39-63.

Marsset, M., Carry, B., Dumas, C., Hanuš, J., Viikinkoski, M., Vernazza, P., Müller, T.G., Delbo, M., Jehin, E., Gillon, M. and Grice, J., 2017. 3D shape of asteroid (6) Hebe from VLT/SPHERE imaging: Implications for the origin of ordinary H chondrites. Astronomy & Astrophysics, 604, p.A64.

Masiero, J.R., Grav, T., Mainzer, A.K., Nugent, C.R., Bauer, J.M., Stevenson, R. and Sonnett, S., 2014. Main-belt asteroids with WISE/NEOWISE: Near-infrared albedos. The Astrophysical Journal, 791(2), p.121.

McCord, T.B., Li, J.Y., Combe, J.P., McSween, H.Y., Jaumann, R., Reddy, V., Tosi, F., Williams, D.A., Blewett, D.T., Turrini, D. and Palomba, E., 2012. Dark material on Vesta from the infall of carbonaceous volatile-rich material. Nature, 491(7422), pp.83-86.

McGraw, L.E., Emery, J.P., Thomas, C.A., Rivkin, A.R., Wigton, N.R. and McAdam, M., 2022. 3 μm Spectroscopic Survey of Near-Earth Asteroids. The Planetary Science Journal, 3(10), p.243.

McSween Jr, H.Y., Emery, J.P., Rivkin, A.S., Toplis, M.J., C. Castillo-Rogez, J., Prettyman, T.H., De Sanctis, M.C., Pieters, C.M., Raymond, C.A. and Russell, C.T., 2018. Carbonaceous chondrites as analogs for the composition and alteration of Ceres. Meteoritics & Planetary Science, 53(9), pp.1793-1804.

McSween Jr, H.Y., Ghosh, A., Grimm, R.E., Wilson, L. and Young, E.D., 2002. Thermal evolution models of asteroids. Asteroids III, 559.

McSween Jr, H.Y., Lauretta, D.S. and Leshin, L.A., 2006. Recent advances in meteoritics and cosmochemistry. Meteorites and the early solar system II, pp.53-66.

Meech, K., Raymond, S.N., Meadows, V., Arney, G., Schmidt, B. and Des Marais, D.G., 2020. Origin of Earth's water: sources and constraints. Planetary Astrobiology, 325.

Migliorini, F., Manara, A., Scaltriti, F., Farinella, P., Cellino, A. and Di Martino, M., 1997. Surface properties of (6) Hebe: A possible parent body of ordinary chondrites. Icarus, 128(1), pp.104-113.

Miyamoto, M., Mito, A., Takano, Y. and Fujii, N., 1981. Spectral reflectance (0.25-2.5 μm) of powdered olivines and meteorites, and their bearing on surface materials of asteroids.
Molnar, L.A., 2011, October. Size and age dependence of Koronis Family colors. In EPSC-DPS Joint Meeting (p. 1684).

Morbidelli, A., Brasser, R., Gomes, R., Levison, H.F. and Tsiganis, K., 2010. Evidence from the asteroid belt for a violent past evolution of Jupiter's orbit. The Astronomical Journal, 140(5), p.1391.

Morbidelli, A., Lambrechts, M., Jacobson, S. and Bitsch, B., 2015. The great dichotomy of the Solar System: Small terrestrial embryos and massive giant planet cores. Icarus, 258, pp.418-429.

Nakajima, M. and Stevenson, D.J., 2014. Investigation of the initial state of the Moon-forming disk: Bridging SPH simulations and hydrostatic models. Icarus, 233, pp.259-267.

Nesvorný, D., Brož, M. and Carruba, V., 2015. Identification and dynamical properties of asteroid families. Asteroids IV, 29, pp.7-321.

Noonan, J.W., Reddy, V., Harris, W.M., Bottke, W.F., Sanchez, J.A., Furfaro, R., Brown, Z., Fernandes, R., Kareta, T., Lejoly, C. and Nallapu, R.T., 2019. Search for the H chondrite parent body among the three largest S-type asteroids:(3) Juno,(7) Iris, and (25) Phocaea. The Astronomical Journal, 158(5), p.213.

O'Brien, D.P., Sykes, M.V. and Tricarico, P., 2011, March. Collision probabilities and impact velocity distributions for Vesta and Ceres. In 42nd Annual Lunar and Planetary Science Conference (No. 1608, p. 2665).

Pahlevan, K. and Stevenson, D.J., 2007. Equilibration in the aftermath of the lunar-forming giant impact. Earth and Planetary Science Letters, 262(3-4), pp.438-449.

Peters, G.H., 1924. Observations of asteroids. The Astronomical Journal, 35, pp.149-153.
Petit, J.M.C., Chambers, J., Franklin, F. and Nagasawa, M., 2002. Primordial excitation and depletion of the main belt.

Pieters, C.M., Goswami, J.N., Clark, R.N., Annadurai, M., Boardman, J., Buratti, B., Combe, J.P., Dyar, M.D., Green, R., Head, J.W. and Hibbitts, C., 2009. Character and spatial distribution of OH/H2O on the surface of the Moon seen by M3 on Chandrayaan-1. Science, 326(5952), pp.568-572.

Prettyman, T.H., Mittlefehldt, D.W., Yamashita, N., Lawrence, D.J., Beck, A.W., Feldman, W.C., McCoy, T.J., McSween, H.Y., Toplis, M.J., Titus, T.N. and Tricarico, P., 2012. Elemental mapping by Dawn reveals exogenic H in Vesta’s regolith. Science, 338(6104), pp.242-246.

Raymond, S.N. and Nesvorny, D., 2020. Origin and dynamical evolution of the asteroid belt. arXiv preprint arXiv:2012.07932.

Rayner, J.T., Toomey, D.W., Onaka, P.M., Denault, A.J., Stahlberger, W.E., Vacca, W.D., Cushing, M.C. and Wang, S., 2003. SpeX: a medium-resolution 0.8–5.5 micron spectrograph and imager for the NASA infrared telescope facility. Publications of the Astronomical Society of the Pacific, 115(805), p.362.

Recht, A.W., 1934. Magnitudes and color indices of asteroids. The Astronomical Journal, 44, pp.25-32.

Redman, R.O., Feldman, P.A. and Matthews, H.E., 1998. High-quality photometry of asteroids at millimeter and submillimeter wavelengths. The Astronomical Journal, 116(3), p.1478.

Reddy, V., Le Corre, L., O'Brien, D.P., Nathues, A., Cloutis, E.A., Durda, D.D., Bottke, W.F., Bhatt, M.U., Nesvorny, D., Buczkowski, D. and Scully, J.E., 2012. Delivery of dark material to Vesta via carbonaceous chondritic impacts. Icarus, 221(2), pp.544-559.

Rivkin, A.S., Howell, E.S., Lebofsky, L.A., Clark, B.E. and Britt, D.T., 2000. The nature of M-class asteroids from 3-μm observations. Icarus, 145(2), pp.351-368.

Rivkin, A.S., Davies, J.K., Clark, B.E., Trilling, D.E. and Brown, R.H., 2001, March. Aqueous alteration on S asteroid 6 Hebe?. In Lunar and Planetary Science Conference (p. 1723).
Rivkin, A.S. and Emery, J.P., 2010. Detection of ice and organics on an asteroidal surface. Nature, 464(7293), pp.1322-1323.

Rivkin, A.S., McFadden, L.A., Binzel, R.P. and Sykes, M., 2006. Rotationally-resolved spectroscopy of Vesta I: 2–4 μm region. Icarus, 180(2), pp.464-472.

Rivkin, A.S., Howell, E.S., Emery, J.P. and Sunshine, J., 2018. Evidence for OH or H2O on the surface of 433 Eros and 1036 Ganymed. Icarus, 304, pp.74-82.

Rubin, A.E. and Bottke, W.F., 2009. On the origin of shocked and unshocked CM clasts in H-chondrite regolith breccias. Meteoritics & Planetary Science, 44(5), pp.701-724.

Sanchez, J.A., Thomas, C., Reddy, V., Frere, N., Lindsay, S.S. and Mitchell, A., 2020. A new method for deriving composition of S-type asteroids from noisy and incomplete near-infrared spectra. The Astronomical Journal, 159(4), p.146.

Shinokawa, K., Takahashi, S., Ogawa, K., Yoshida, F., Minato, T., Mukai, T. and Kawabata, K., 2002. Observations of photopolarimetric variation with the rotation of asteroids, 3 Juno and 216 Kleopatra. Memorie della Società astronomica italiana, 73, p.658.

Spoto, F., Milani, A. and Knežević, Z., 2015. Asteroid family ages. Icarus, 257, pp.275-289.

Storrs, A.D., Dunne, C., Conan, J.M., Mugnier, L., Weiss, B.P. and Zellner, B., 2005. A closer look at main belt asteroids 1: WF/PC images. Icarus, 173(2), pp.409-416.

Strom, C.A., Fieber-Beyer, S.K., Gaffey, M.J. and Germann, J.T., 2021, March. A Spectral Analysis of the Massalia Asteroid Family to Evaluate the L-Chondrite Source Hypothesis. In 52nd Lunar and Planetary Science Conference (No. 2548, p. 1597).

Sunshine, J.M., Bus, S.J., McCoy, T.J., Burbine, T.H., Corrigan, C.M. and Binzel, R.P., 2004. High-calcium pyroxene as an indicator of igneous differentiation in asteroids and meteorites. Meteoritics & Planetary Science, 39(8), pp.1343-1357.

Sunshine, J.M., Farnham, T.L., Feaga, L.M., Groussin, O., Merlin, F., Milliken, R.E. and A'Hearn, M.F., 2009. Temporal and spatial variability of lunar hydration as observed by the Deep Impact spacecraft. Science, 326(5952), pp.565-568.

Svetsov, V., 2011. Cratering erosion of planetary embryos. Icarus, 214(1), pp.316-326.

Takahashi, J., Itoh, Y. and Takahashi, S., 2011. Mid-infrared spectroscopy of 11 main-belt asteroids. Publications of the Astronomical Society of Japan, 63(3), pp.499-511.

Takir, D. and Emery, J.P., 2012. Outer main belt asteroids: Identification and distribution of four 3-μm spectral groups. Icarus, 219(2), pp.641-654.

Takir, D., Reddy, V., Sanchez, J.A., Shepard, M.K. and Emery, J.P., 2016. Detection of water and/or hydroxyl on asteroid (16) Psyche. The Astronomical Journal, 153(1), p.31.

Taylor, S., Lever, J.H. and Harvey, R.P., 2000. Numbers, types, and compositions of an unbiased collection of cosmic spherules. Meteoritics & Planetary Science, 35(4), pp.651-666.

Tedesco, E.F., P.V. Noah, M. Noah, and S.D. Price. IRAS Minor Planet Survey. IRAS-A-FPA-3-RDR-IMPS-V6.0. NASA Planetary Data System, 2004

Thomas, C.A., Emery, J.P., Trilling, D.E., Delbó, M., Hora, J.L. and Mueller, M., 2014. Physical characterization of Warm Spitzer-observed near-Earth objects. Icarus, 228, pp.217-246.

Tikoo, S.M. and Elkins-Tanton, L.T., 2017. The fate of water within Earth and super-Earths and implications for plate tectonics. Philosophical Transactions of the Royal Society A: Mathematical, Physical and Engineering Sciences, 375(2094), p.20150394.

Ueda, Y., Hiroi, T., Pieters C. M., Miyamoto M., (2002) Changes of Band I center and Band II/Band I area ratio in reflectance spectra of olivine-pyroxene mixtures due to the space weathering and grain size effects. Lunar Planet. Sci. XXXIII, Abstract #2023.

Vacca, W.D., Cushing, M.C. and Rayner, J.T., 2003. A Method of Correcting Near-Infrared Spectra for Telluric Absorption1. Publications of the Astronomical Society of the Pacific, 115(805), p.389.MacLennan, E. 2019, PhD dissertation, Univ. Tennessee, https://trace. tennessee.edu/utk_graddiss/5467

Vereshchagina, I.A., Gorshanov, D.L., Devyatkin, A.V. and Papushev, P.G., 2009. Some specific features of light curves of (39) Laetitia,(87) Sylvia,(90) Antiopa, and 2006 VV2 asteroids. Solar System Research, 43(4), pp.291-300.

Vernazza, P., Carry, B., Emery, J., Hora, J.L., Cruikshank, D., Binzel, R.P., Jackson, J., Helbert, J. and Maturilli, A., 2010. Mid-infrared spectral variability for compositionally similar asteroids: Implications for asteroid particle size distributions. Icarus, 207(2), pp.800-809.

Veverka, J., 1973. Polarimetric observations of 9 Metis, 15 Eunomia, 89 Julia, and other asteroids. Icarus, 19(1), pp.114-117.

Vokrouhlický, D., Brož, M., Bottke, W.F., Nesvorný, D. and Morbidelli, A., 2006. Yarkovsky/YORP chronology of asteroid families. Icarus, 182(1), pp.118-142.

Walsh, K.J., Morbidelli, A., Raymond, S.N., O'Brien, D.P. and Mandell, A.M., 2011. A low mass for Mars from Jupiter's early gas-driven migration. Nature, 475(7355), pp.206-209

Wamsteker, W. and Sather, R.E., 1974. Minor planets and related objects. XVII-Five-color photometry of four asteroids. The Astronomical Journal, 79, pp.1465-1470.

Warner, B.D., Harris, A.W., and Pravec, P., Asteroid Lightcurve Data Base (LCDB) Bundle V4.0. urn:nasa:pds:ast-lightcurve-database::4.0. NASA Planetary Data System, 2021; doi: 10.26033/j3xc-3359

Williams, J.G., 1992. Asteroid families—An initial search. Icarus, 96(2), pp.251-280.
Wood, J.A., 2005, December. The chondrite types and their origins. In Chondrites and the protoplanetary disk (Vol. 341, p. 953).

Wordsworth, R.D., 2016. The climate of early Mars. Annual Review of Earth and Planetary Sciences, 44, pp.381-408.

Wray, J.J., 2021. Contemporary liquid water on Mars?. Annual Review of Earth and Planetary Sciences, 49, pp.141-171.

Wu, J., Desch, S.J., Schaefer, L., Elkins-Tanton, L.T., Pahlevan, K. and Buseck, P.R., 2018. Origin of Earth's water: chondritic inheritance plus nebular ingassing and storage of hydrogen in the core. Journal of Geophysical Research: Planets, 123(10), pp.2691-2712.

Yoshikawa, M., Fujiwara, A., Kawaguchi, J. and Mission, H., 2006. The nature of asteroid Itokawa revealed by Hayabusa. Proceedings of the International Astronomical Union, 2(S236), pp.401-416.

Young, E.D., Ash, R.D., England, P. and Rumble III, D., 1999. Fluid flow in chondritic parent bodies: Deciphering the compositions of planetesimals. Science, 286(5443), pp.1331-1335.

Young, E.D., Zhang, K.K. and Schubert, G., 2003. Conditions for pore water convection within carbonaceous chondrite parent bodies–implications for planetesimal size and heat production. Earth and Planetary Science Letters, 213(3-4), pp.249-259.

Zellner, B., 1979. The Tucson revised index of asteroid data. In Asteroids (pp. 1011-1013). Univ. of Arizona Press Tucson.

Appendix 1: Mineralogy inferred from near-infrared spectroscopy

To determine the relative abundances of minerals in the dataset gathered, we begin by preforming band parameter analyses to determine the centers and depths of the 1- and 2-μm bands, band area ratio and associated errors with each measurement. The following methodology was used to calculate each element.

Prior to the band parameter analysis, we implemented a temperature correction for the 2-μm band. Temperature can affect near-infrared bands for asteroids with significant mafic materials on their surfaces (e.g., Sanchez et al., 2012 and references therein). These induced effects can cause the 2-μm band's position, width and depth to shift. We use the methodology from Sanchez et al., (2012) to empirically correct the 2-μm band (Band II, or BII) using this equation:

$$\Delta BII\ (\mu m) = 0.06 - 0.0002\ \times T(K).$$

Methodology.

As stated above, the prism data for these S-complex asteroids typically have two distinct bands, one at 1- and the other at 2-μm. We call the 1-μm band 'Band I' and the 2-μm band 'Band II'. To summarize, the band parameter analysis utilizes smoothed, continuum removed spectral segments of the 1-μm and 2-μm bands to determine the band centers, depths, and areas of Band I and Band II. The Band Area Ratio is defined as the quotient of Band II and Band I.

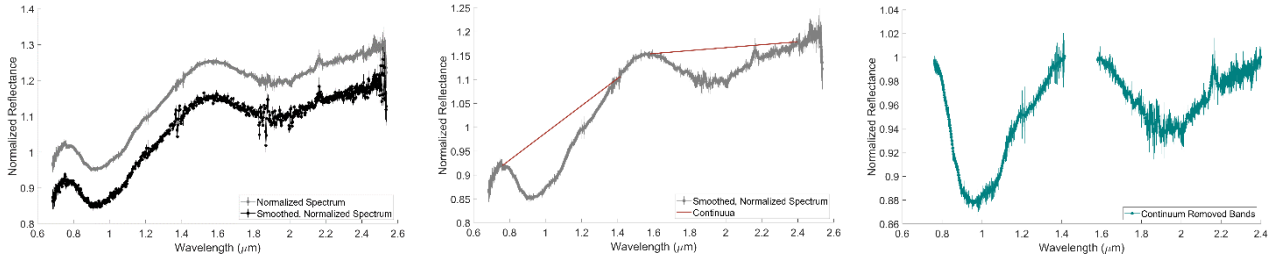

A1.F1: Defining spectral segments. (left) prism data (black) are first smoothed (gray spectrum offset by 0.1 for clarity) then (middle) continua are defined as the local maximum ~0.75-μm and the 'roll over' location or the local maximum near ~1.5μm. Finally, (right) the continua are divided from the spectral segments and the band positions, depths and areas are subsequently calculated.

Spectral Segments:

The band parameter analysis begins with defining the segments of each spectrum where Band I and Band II occur. The spectrum is passed to a function that smooths the data over a 0.036-μm window. The smoothing function returns an average value in a given window using a quadratic regression. Next, the end points of Band I and Band II are determined. Looking at an exemplary prism spectrum (**Figure A1.F1**) there appear to be two local maxima around Band I. The first local maximum appears around 0.75-μm and the other appears around 1.5-μm. The data within ~0.5-μm of each maxima are fitted with a cubic polynomial and then the position of the each maximum is determined by finding the peak of the polynomial function. The starting point of Band I is defined as the peak of the fitted polynomial around 0.75-μm. The end point of Band I is sometimes the peak of the fitted polynomial ~1.5-μm. However, Band I can sometimes terminate before this point.

For a number of asteroids in this sample we find that a continuum between the starting point of the Band I spectral segment and the local maximum ~1.5-μm sometimes crosses the data somewhere between 1.1 and 1.4-μm. This is defined as the 'roll over' index because the data 'rolls over' the continuum. Using methodology consistent with Thomas et al., (2014), we define the Band I end point as the spot where the continuum drawn between the two local maxima around Band I intersects the spectrum itself.

Band II is determined by the position of the fitted polynomial for the local maximum ~1.5-μm and 2.4-μm. For all of the data in our study, we use the end point as 2.4-μm. Typically, the noise in the prism data gets very large at the end of the detector due to edge effects so we exclude everything longer that 2.4-μm avoid the spuriously noisy data points.

Once the data has been smoothed and the Band I and Band II spectral segments have been defined, we perform a continuum removal of the data. The Band I and Band II continua are defined as straight lines between the end points of each segment. Band I and Band II spectral segments are then divided by the continuum, removing any effects of spectral slope from the underlying band parameters (Right most panel in **A1.F1**).

Using the methodology described in Sanchez et al., (2020), we determine Band I center. To briefly summarize, we select subsets of the Band I spectral segment with different starting and ending wavelengths and fit 3rd and 4th order polynomials to each portion of the smaller segment. We determine the position of the minima of each polynomial. The center position of Band I is defined as the mean of all the minima positions and the error of this parameter is defined as the standard deviation of the minima positions.

The Band II center position is determined in a similar way to Band I. However, we utilize 2nd and 3rd order polynomials because this band is typically wider than Band I. The position and errors are the mean and standard deviation of the fitted minima, as for Band I.

Band I and Band II depths are calculated using a similar methodology described in Thomas et al., (2014). We take the difference between the continuum and the continuum removed spectrum at the position of the band center. We define this as the band depth. To determine the error of this measurement, we modify the value of the spectrum at the band center position with the error of the spectrum at that point and a random number generated over the value of [-1 1]. We repeat this process 20,000 times then take a standard deviation of the synthetic band depths to estimate the error.

Band areas are determined using the trapezoidal method. The errors for this parameter also utilize the methods of Thomas et al., (2014), which are similar to the band depth error generation. Here we modify each point along the spectrum with the error of the spectrum and a random number generated over the range of [-1, 1]. We calculate the synthetic area using the same trapezoidal function, generating 20,000 synthetic areas. The error is defined as the standard deviation of the synthetic areas. The band area ratio is the quotient of Band II area to Band I area.

We impose a minimum error on each measurement to account for systematic uncertainties in the measurements, consistent with the approach in Thomas et al., (2014) and references therein. All the errors in the band parameter tables are quoted with these errors unless the error is larger than that threshold. Band centers have a minimum error of 0.01, band areas have a minimum error of 0.07 and band area ratio have minimum error of 0.1.

The band parameters for each object are presented in **A1.T1.**

Mineralogy Discussion

Comparison to Literature

As we discussed in Section 2.3, some of the asteroids presented here have been observed previously with a variety of techniques. We will discuss now our mineralogy results that we derive from near-infrared spectroscopy with previously published results.

Gaffey et al., (1993) presented spectra for a large number of the objects we observed. We report different interpretations of S-type subclass for most of the objects observed in both studies. Beginning with the similarities, we find that five of our interpretations of S-type subclass are consistent with Gaffey et al., (1993) [(3) Juno, (6) Hebe, (7) Iris, (20) Massalia, (67) Asia].

Most of the asteroids we interpret differently to Gaffey et al., (1993) are quite close in parameter space to the Gaffey et al., (1993) reported band parameters [including, (9) Metis, (11) Parthenope, (33) Polyhymnia, (63) Ausonia, (82) Alkmene, (115) Thyra, (364) Isara]. For example, (11) Parthenope in our work is interpreted to be an SIII subclass object. It appears just leftward of the left of the SIV field in the Band I center vs. band area ratio plot. SIV subclass was the assignment for Parthenope in Gaffey et al., (1993). This suggests that differences in observing conditions, observing geometry, signal-to-noise between the observations, advances in instrumentation between this work and that of Gaffey et al., (1993), or choice of endpoints for the band parameter analysis (e.g., Sanchez et al., 2020) are the likely cause of these minor differences.

One object, however, is significantly different. Our spectrum of Melpomene is quite different from the one presented in Gaffey et al., (1993). The difference between our spectrum of Melpomene and the one in Gaffey et al., (1993) might indicate significant parent body heterogeneity on this asteroid.

Potential parent body heterogeneity

We obtained multiple observations of three asteroids, (14) Irene, (17) Thetis and (182) Elsa. Each observation of the asteroids resulted in a different interpretation of the underlying mineralogy.

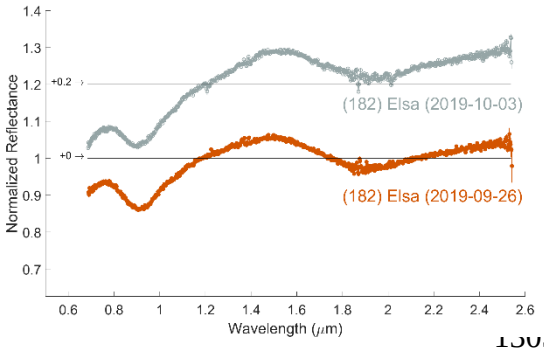

A1.F2: Elsa spectra observed ~1 week apart. Elsa appears to have surface composition heterogeneity.

Elsa was observed twice (**A1.F2**), eight days apart in Fall of 2019. Elsa has a very long rotation period (~80 hours), so the elapsed time between the two observations represents ~2.1375 rotations periods. The two prism observations indicate either a basaltic achondrite mineralogy or an SVI field mineralogy. The band area ratio values differ significantly (1.71+/-0.0061 and 1.50 +/- 0.0049 respectively) and the Band I centers are very close in value (0.921-µm and 0.926-µm). Because Elsa was observed so close in time, the observational

circumstances are very similar; the phase angle in particular only changes between the two observations by 0.6 degrees. Given this information, it seems possible that Elsa may have some rotational heterogeneity on its surface. The Basaltic Achondrite and SVI fields are close together in the Gaffey plot parameter space; it seems reasonable that heterogeneity exists on this asteroid.

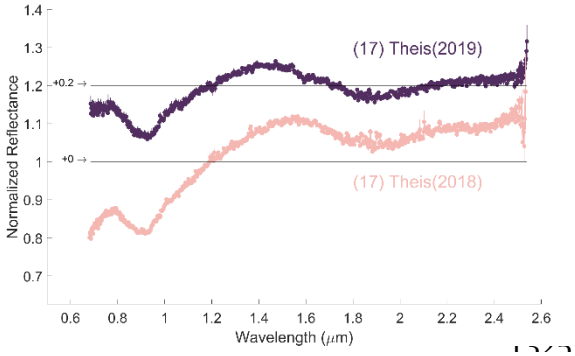

A1.F3: Thetis spectra.

Asteroid (17) Thetis (**A1.F3**) was also observed twice in the course of this project. However, these observations were made ~150 days apart. The second observation was made when the distance between the asteroid and the Earth was significantly smaller, and the phase angle was much smaller in the later observation as well. Still, the band parameters are somewhat similar between the two objects: band area ratios values differ most significantly (1.007 and 1.188); Band I centers are virtually identical (0.926 and 0.926). We interpret the 2019 observation of Thetis to be consistent with a primitive achondrite mineralogy based on the difference between the Band II centers between the observations (1.9 +/- 0.053-µm and 1.87+/- 0.038-µm). Further analysis in **Appendix 2** (e.g., **A2.F1**) shows that the second observation of Thetis is right on the border between the primitive achondrite field and the H chondrite field. The uncertainty on the Band II center could indicate a H chondrite mineralogy. The interpretation of Thetis presented in Sunshine et al., (2004) indicates the presence of high calcium pyroxene and therefore partial differentiation on this object. The second observation of Thetis is consistent with the finding from Sunshine et al., (2004). However, grain size and/or space weathering may also affect band parameters by causing subtle changes in an asteroid's spectrum (e.g., Ueda et al., 2002). We conclude that (17) Thetis appears to have rotational heterogeneity. Thetis's surface may have mechanical heterogeneity (e.g., grain size differences), relative difference of surface age or potentially a compositional difference with some parts of the surface showing evidence of partial differentiation. More observations are needed to confirm this heterogeneity and its cause.

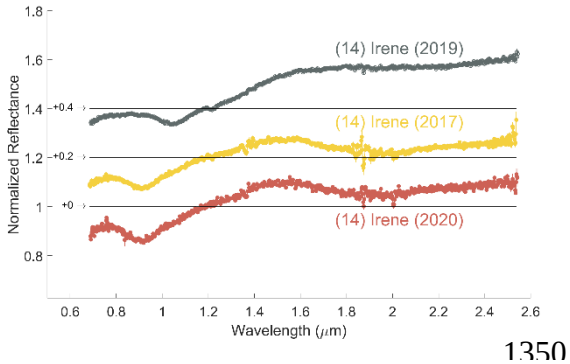

A1.F4: Irene spectra.

(14) Irene was observed on three separate occasions during data collection (**Figure A1.F4),** once in each of the following years: 2017, 2019 and 2020. Looking at the spectra, it seems Irene has three distinct mineralogies: an H ordinary chondrite-like spectrum (2020), an intermediate mineralogy (2017) and a basaltic achondrite mineralogy (2019) on the same asteroid. Further investigations of this potential heterogeneity are necessary.

Appendix 2: Identifying Asteroids compositionally similar to Ordinary Chondrite Subtypes

Studies of ordinary chondrites show that each ordinary chondrite subtypes (H, L and LL) have highly clustered geochemical and petrologic signatures (e.g., total iron abundance, distribution of iron between metal and silicates, disparate clasts, oxygen isotopes etc., [e.g., Dodd, 1981]). These clustered signatures allow ordinary chondrites to be categorized into different subtypes. The interpretation of these multiple subtypes in the ordinary chondrite group is that each ordinary chondrite subtype could have formed on a single parent body. Given what we know of planet formation, it is more likely that ordinary chondrite subtype groups are sourced from populations of asteroids that formed very close in time and space to each other such that their initial chemical compositions, including short-lived radioactive nuclei abundance, were similar (e.g., Wood, 2005). As a consequence of these similar initial formation conditions, these groups of objects experienced similar parent body evolution resulting in a population of meteorites that are petrologically identical even if not sourced from the exact same object.

Using the methodologies in Dunn et al., (2010) and Sanchez et al., (2020), we can determine the similarity between the ordinary chondrite-like asteroids with each of the three subtypes. First it is necessary to investigate whether any of the objects in this study are related to primitive achondrites which can plot in the same region as ordinary chondrites in the Gaffey plot.

Lucas et al., (2019) showed that acapulcoite-lodranite clan meteorites plot in the SIV parameter space on the Gaffey plot, yet they are compositionally distinct from ordinary chondrites. It appears that the acapulcoite-lodranite clan meteorites formed from a chondritic precursor then experienced heating to the point of silicate melting. These parent bodies did not experience full differentiation but rather partial melting which affected the textures and compositions of the precursor materials. The acapulcoite-lodranite clan meteorites come from distinct parent bodies to the ordinary chondrites. Ordinary chondrites experienced heating resulting in thermal metamorphism evident in the textures and composition of these meteorites.

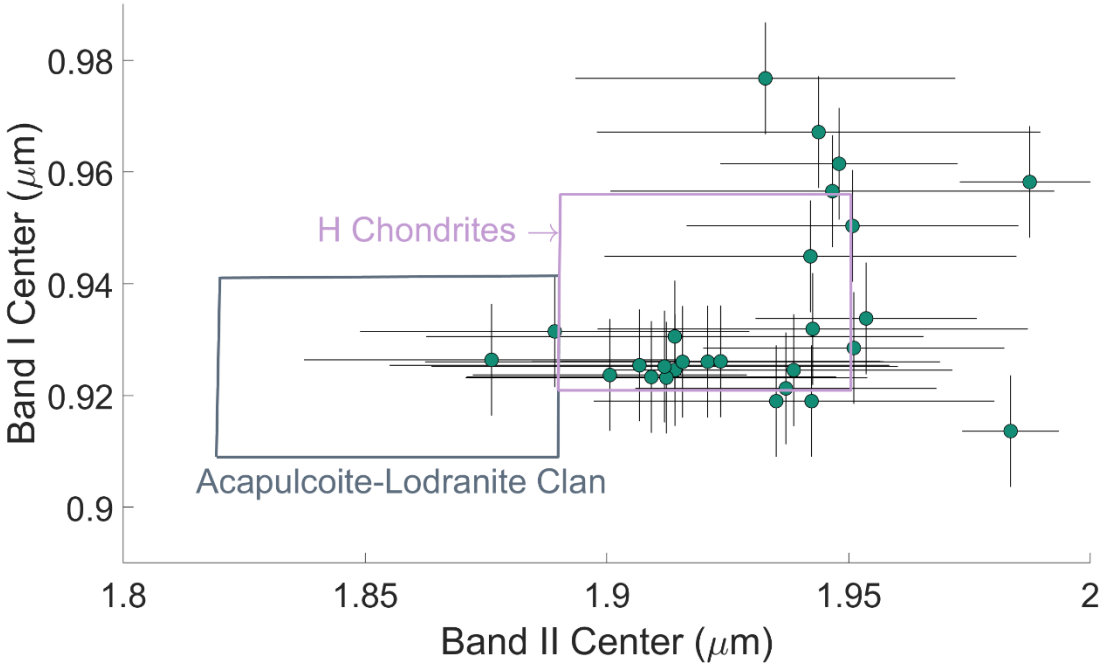

A2.F1: Band I center vs. Band II center for the S-type asteroids observed. This plot is based on the work of Lucas et al., (2019) where primitive achondrites in the acapulcoite-lodranite clan can be distinguished from H ordinary chondrites. Both groups of meteorites appear in the ordinary chondrite boot of the Gaffey et al., 1993 plot. Using the Band I vs. Band II centers allows us to distinguish any asteroids that may have experienced partial melting. We find two potential acapulcoite-lodranite clan asteroids: (277) Elvira and (17) Thetis (2018). The Thetis band centers are on the boundary with H ordinary chondrites but still may represent unequilibrated and partially melted lithologies on the same object.

Lucas et al., (2019) show that the acapulcoite-lodranite clan meteorites are distinct from ordinary chondrites in the Band I center vs. Band II center parameter space. The acapulcoite-lodranite clan meteorites exhibit lower ferrous iron content in both the olivines and pyroxenes present compared to H ordinary chondrites. This compositional difference reveals itself in the Band I center vs. Band II center parameter space where H chondrites have Band II centers at longer wavelengths compared to the less iron rich acapulcoite-lodranite clan meteorites. Similarly, the Band I centers for H chondrites are at a slightly longer wavelength again owing to the iron content compared to acapulcoite-lodranite clan meteorites.

Considering this parameter space for our asteroids (**A2.F1**), we find that two of the SIV objects plot in the lower-iron region in the Band I center vs. Band II center, indicating that these objects, (277) Elvira and (17) Thetis (observed in 2019), are likely partially melted primitive achondrites rather than ordinary chondrites. Their spectra are presented in **A2.F2**. However, particle size and space weathering can subtly shift band parameters (e.g., Ueda et al., 2002). Without any a priori knowledge about the surface age or grain size on the surfaces of the two potential acapulcoite-lodranite clan-like asteroids, and given the relative size of the error on the measurements, it is possible both (277) Elvira and (17) Thetis are consistent with H-ordinary chondrite mineralogy. We exclude them from the remaining analysis out of an abundance of caution.

Taking the remaining 15 objects which are likely ordinary chondrite like (rather than achondritic), we now attempt to determine the subtype of each asteroid.

In their systematic spectral-mineralogical study, Dunn et al., (2010) show that abundance of olivine (ol/ol+px) and the relative abundance of fayalite and ferrosilite can be derived using Band I/II centers and areas. When the derived olivine and ferrosilite/fayalite abundances are plotted, each ordinary chondrite subclassification can be distinguished. We will describe how each of these quantities are derived and present our analysis of these data.

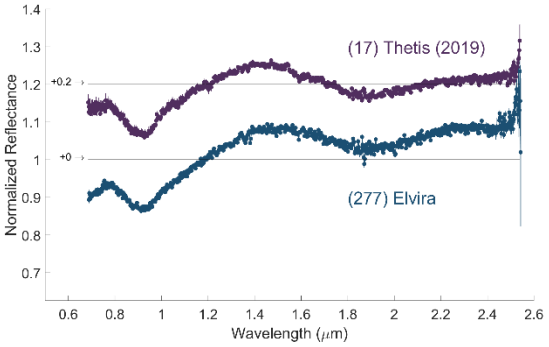

A2.F2: Acapulcoite-Lodranite-like asteroids. (17) Thetis (observed in 2019) and (277) Elvira are spectrally consistent with the partially melted achondrites in the acapulcoite-lodranite clan (Lucas et al., 2019). This indicates these objects might not be ordinary chondrite like but represent asteroids that experienced different parent body processing.

Dunn et al., (2010) provide empirical relationships based on band parameters and compositions derived through XRD analyses of the ordinary chondrites in their sample. Sanchez et al., (2020) returned to their analyses but explored how signal-to-noise ratio and wavelength range affect these empirical relationships. Typically, telescopic data does not cover the same wavelength range as laboratory data and telescopic data has lower signal-to-noise. These so-called "incomplete datasets" yield different band parameters than laboratory data which is related to the wavelength range and signal-to-noise of the observations. Using the updated Sanchez et al., (2020) empirical relationships that are relevant to the wavelength range of prism data, we determine the olivine-pyroxene abundance ratio as well as molar content of ferrosilite and fayalite for our objects using these empirical relationships:

$$\frac{ol}{ol+px} = -0.2053 \times BAR + 0.709,$$

$$Fa = -1283.4 \times BIC^2 + 2609.5 \times BIC - 1295.8,$$

$$Fs = -904.4 \times BIC^2 + 1837.3 \times BIC - 907.7.$$

Here BAR stands for band area ratio and BIC is the Band I center position. Plotting the olivine-pyroxene abundance ratio against the modal abundance of fayalite and separately, the modal abundance of ferrosilite allows us to determine ordinary chondrite subclassification for the asteroids in our dataset (**A2.F3)**. We find that a significant fraction of our SIV asteroids are consistent with H ordinary chondrite mineralogy (7 of the 15 objects). Two asteroids are consistent with either H or L chondrite mineralogy; one asteroid appears to be L-chondrite like while three are LL-chondrite like. We also have two asteroids that could be either L or LL chondrite like.

The modal mineralogies for the H ordinary chondrite like asteroids are presented in **A2.T1**.

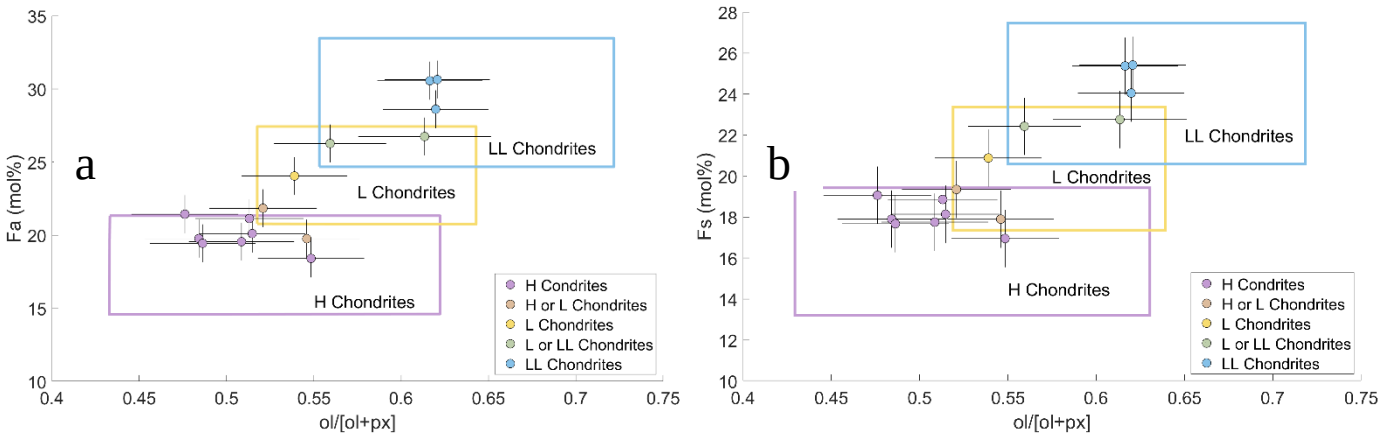

A2.F3: (a) abundance of olivine vs. fayalite abundance derived from band parameter analysis. (b) abundance of olivine vs. ferrosilite abundance. Asteroids that plot in the ordinary chondrite boot are compared to their relative abundance of fayalite, ferrosilite and total olivine based on the analysis of Dunn et al., (2010) with the refinements of the original empirical relationships for mineralogy from Sanchez et al., (2020). We see that the ordinary chondrite like asteroids have similarities to H, L and LL chondrites. The subtyping of the asteroids is listed in Table 4 and 5.

The olivine abundances for the ordinary chondrite-like asteroids are generally lower in value compared to the abundances derived from visible/near-infrared spectroscopy (Iris, Isara). Vernazza et al. (2010) report 76.5% and 77% respectively for [ol/ol+px] values comparted 61+/-3% and 62+/-3%. This difference may be related to the fact that we do not have visible wavelengths as a part of our analysis. Subtle differences between end-points and signal-to-noise ratios can change the derived quantities (e.g., Sanchez et al., 2020). Taking an average value of the Vernazza et al., (2010) results based on the derived olivine abundances using all techniques (e.g., visible-near-infrared spectroscopy and two derivations with different mid-infrared observations), our values are roughly consistent with theirs.

The mineralogy of Iris was reported to be LL ordinary chondrite-like (Noonan et al., 2019). Our results are in agreement. Those authors also presented a spectrum and interpretation of (3) Juno. Here our results differ: Noonan et al., (2019) find June to be similar to H ordinary chondrites.

We find Juno to be more consistent with L or LL lithologies. Juno is known to have a heterogenous surface (e.g., Degewij et al., 1979; Shinokawa et al., 2002) with one likely significant impact crater (Baliunas et al., 2003). It is possible that the impact event emplaced material of different composition on the surface, which could result in the observed heterogeneity between this work and that of Noonan et al., (2019).

Tables

Table 1: Observation Circumstances

Object	*Date*	*V*	*standard star*	*LXD midtime*	*integration time*	*# images*	*Prism mid time*	*integration time*	*# images*	*weather (seeing [arcseconds])*	*rh*	*delta*	*phase*
3 Juno	11/17/2018		HD23030	9:17	830	68	n.a.	n.a.	n.a.	not reported	1.98	1.04	11.27
5 Astrea	2/3/2020		HD 62346	12:15	300	40	11:08	24	8	0.64	2.09	1.13	7.48
6 Hebe	12/18/2018		HD46055	14:20	960	64	15:24	180	36	0.5	2.20	1.26	9.99
7 Iris (2018-12-13)	12/13/2018		HD109130	15:27	960	64	14:19	42	10	0.472	2.64	2.78	20.7
8 Flora	12/27/2017		HD 268518	11:55	240	32	n.a.	n.a.	n.a.	0.84	2.01	1.03	4.43
9 Metis	10/3/2019		BD+03 324	14:46	480	32	14:15	46	18	0.83 (intermittent fog)	2.18	1.24	12.6
11 Parthenope	5/14/2019		HD 140460	10:14	960	64	9:04	64	16	1.05	2.42	1.42	3.16
14 Irene (2019-10-03)	10/3/2019		HD12356	12:56	660	64	13:50	140	16	0.83 (intermittent fog)	2.99	2.04	6.91
14 Irene (2020-02-03)	2/3/2020		HD 9595	6:39	1110	74	5:23	60	4	0.4	2.89	3.06	18.79
Irene (2017-02-15)	2/15/2017		HD 93215	12:02	630	52	10:33	24	16	not reported	2.21	1.24	6.76
17 Thetis (2018-12-16)	12/16/2018		HD 104770	14:43	420	56	13:50	240	8	0.68	2.51	2.41	22.93
17 Thetis (2019-03-15)	3/15/2019		BD+62574	12:44	960	64	11:32	15	10	0.632	2.38	1.40	4.96
18 Melpomene	7/4/2019		HD 172317	9:34	960	64	8:36	check header	8	0.71	2.26	1.26	6.38
20 Massalia	12/27/2017		HD 35769	10:45	180	24	9:50	24	8	0.84	2.07	1.10	5.57
30 Urania	9/18/2018		SA115271	11:01	930	62	9:59	60	10	clear	2.12	1.11	1.54

33 Polyhymnia	10/9/2019	HD8233	9:08	630	42		111	18		0.67	1.99	0.99	3.48
39 Laetitia	8/26/2019	HD202954	9:50	630	42	8:45	34	22		0.55	2.53	1.52	4.38
63 Ausonia	4/23/2017	HD111546	9:37	1140	76	7:45	280	14		1	2.25	1.27	7.11
67 Asia	5/2/2019	HD 113763	7:18	720	80	5:38	120	8		1	2.43	1.46	8.96
82 Alkmene	2/10/2017	BD+19 2241	11:55	180	86	10:15	110	12		0.65	2.16	1.18	2.14
103 Hera (2020-09-20)	9/20/2019	HD 225211	11:18	540	72	10:08	80	8	cloudy		2.52	1.51	2.34
115 Thyra (prism)	9/7/2018	HD213275	n.a.	n.a.	n.a.	8:26	40	8		1.33			
115 Thyra (LXD)	3/6/2020	HD 94723	10:10	1080	72	n.a.	n.a.	n.a.		0.8	2.55	1.57	4.66
151 Abunditia	3/15/2019	HD104925	14:28	960	64	15:23	300	10		0.632	2.51	1.52	4.02
182 Elsa (2019-10-03)	9/26/2019	HD 472	8:52	960	64	7:10	240	16	0.83 (intermittent fog)		2.09	1.09	3.03
182 Elsa (2020-09-26)	10/3/2019	HD2691	10:50	660	44	10:12	200	16	clear		2.10	1.10	2.43
208 Lacrimosa	2/17/2019	HD 87776	12:12	2400	160	10:00	345	12		1.1	2.86	1.88	1.15
277 Elvira	9/23/2017	bd-04 5927	10:35	2040	136	12:45	450	20		0.5	2.62	1.62	1.54
352 Gisela	2/25/2020	PPM 156693	10:58	1680	112	12:15	150	10		0.65	2.34	1.36	2.57
364 Isara	10/12/2017	HD12356	11:50	1320	88	10:35	360	8		0.45	1.94	0.95	7.63
462 Eriphyla	10/30/2017	HD13303	9:49	1830	122	7:40	360	12		0.44	2.67	1.68	1.81
703 Noemi (2019-09-25)	9/25/2019	HD224448	10:00	4320	144	14:18	300	10	0.48, improving to 0.3		2.30	3.29	0.59
808 Merxia (2017-03-03)	3/3/2017	HD97441	10:15	1590	122	7:56	300	12		0.91	2.59	1.61	2.59
913 Otila	5/19/2020	HD 138186	9:57	2880	192	13:11	300	12		0.195	1.91	0.91	4.55

Table 2: Thermal Model Parameters

Object	*V-band/K-band**	*Beaming Parameter*	*Reflectance at 2.45-µm*	*Continuum slope (μm^{-1})*	*T (K)*
3 Juno					299.17
5 Astrea	1.11	0.7	1.02		296.91
6 Hebe	1.235	0.8	1.025	0.04	280.18
7 Iris (2018-12-13)	1.235	0.9	1.1		248.34
8 Flora	1	0.9	1.005	0.025	284.83
9 Metis	1.35	0.8	1.035		286.05
11 Parthenope	1.22	1	1.035	0.05	254.92
14 Irene (2019-10-03)	1.17	0.7	1.025	0.035	236.21
14 Irene (2020-02-03)	1.21	0.7	1.06	0.04	255.92
Irene (2017-02-15)	1.275	0.7	1.025		292.48
17 Thetis (2018-12-16)	1.5	1.2	1.06		225.96
17 Thetis (2019-05-15)	1.11	0.8	1.02	0.04	271.54
18 Melpomene	1.76	**0.9**	1.07		299.01
20 Massalia	1.235	0.9	1		279.97
30 Urania	1.375	0.9	1.06	0.15	279.75
33 Polyhymnia	1.25	1.1	1.1		270.48
39 Laetitia	1.257	0.75	1.05	0.08	266.18
63 Ausonia	1.4375	0.9	1.03	0.1	272.61
67 Asia	1.17	0.7	1.055	0.025	263.83
82 Alkmene	1.02	0.75	1.025		289.48
103 Hera (2020-09-20)	1.29	0.9	1		249.35
115 Thyra	1.17	0.8	1.01	0.02	260.81
151 Abunditia	1.54	1.2	1.03	0.01	273.9
182 Elsa (2019-10-03)	1.33	0.9	1.05		305.42
182 Elsa (2020-09-26)	1.15	0.7	1.03	0.055	280.77

208 Lacrimosa	1.33	0.7	1.1		255.81
277 Elvira	1.235	0.7	1.05	0.05	267.49
352 Gisela	1.5	0.9	1.035		273.77
364 Isara	1.54	0.9	1.07		308.03
462 Eriphyla	1.29	1.6	1.2	0.05	214.25
703 Noemi (2019-09-25)	1.33	0.7	1.12		282.71
808 Merxia (2017-03-03)	1.125	0.9	1.17	0.03	252.21
913 Otila	1.16	1	1.1	0.05	337.75
115 Thyra (PRISM only)	na	**Na**	na	na	na

* V-band/K-band is the ratio of reflectance at 0.55 μm to the reflectance at 2.2 μm.

Slope of the continuum used for thermal tail correction and 3-um band calculation.

Table 3: Physical & Orbital Properties

Object	*H*[1]	*G*	*albedo*	*D(km)*	*rotation period (hours)*[2]	*SMASS II*	*Tholen*
3 Juno	5.3	0.32	0.21[3]	246.6[3]	7.21	Sk	S
5 Astrea	6.9	0.15	0.27[3]	106.7[3]	16.81	S	S
6 Hebe	5.8	0.24	0.24[4]	185.2[4]	7.27	S	S
7 Iris (2018-12-13)	5.6	0.15	0.28[4]	199.8[4]	7.14	S	S
8 Flora	6.5	0.28	0.23[3]	147.5[3]	12.87		S
9 Metis	6.3	0.17	0.12[5]	190[6]	5.08		S
11 Parthenope	6.5	0.15	0.19[3]	142.9[3]	13.72	Sk	S
14 Irene (2019-10-03)	6.5	0.15	0.16[5]	152[6]	15.03	S	S

14 Irene (2020-02-03)	6.5	0.15	0.16	152	15.03	S	S
Irene (2017-02-15)	6.5	0.15	0.16	152	15.03	S	S
17 Thetis (2018-12-16)	7.7	0.15	0.19[3]	84.9[3]	12.27	Sl	S
17 Thetis (2019-05-15)	7.7	0.15	0.19	84.9	12.27	Sl	S
18 Melpomene	6.6	0.25	0.18[3]	139.6[3]	11.57	S	S
20 Massalia	6.5	0.25	0.24[3]	135.7[3]	8.1	S	S
30 Urania	7.5	0.15	0.19[3]	92.8[3]	13.69	Sl	S
33 Polyhymnia	8.5	0.33	0.24[3]	52.9[3]	18.61	Sq	S
39 Laetitia	6.1	0.15	0.27[3]	179.5[3]	5.15	S	S
63 Ausonia	7.4	0.25	0.13[3]	116[3]	9.30	Sa	S
67 Asia	8.3	0.15	0.1[3]	56.3[3]	15.85	S	S
82 Alkmene	8.2	0.28	0.17[3]	57.6[3]	12.99	Sq	S
103 Hera (2020-09-20)	7.6	0.15	0.22[3]	83.9[3]	23.74	S	S
115 Thyra	7.6	0.12	0.27[4]	79.8[4]	7.21	S	S
151 Abunditia	9.2	0.15	0.19[3]	39[3]	9.86	Sl	S
182 Elsa (2019-10-03)	9.1	0.15	0.20[3]	39.5[3]	80.09	S	S
182 Elsa (2020-09-26)	9.1	0.15	0.20	39.5	80.09	S	S
208 Lacrimosa	9.2	0.15	0.21[3]	40.1[3]	14.09	Sk	S
277 Elvira	9.9	0.15	0.20[3]	30.4[3]	29.69		S
352 Gisela	10.1	0.15	0.20[3]	26.7[3]	7.49	Sl	S
364 Isara	9.9	0.15	0.30[3]	25.9[3]	9.16		S
462 Eriphyla	9.4	0.15	0.26[3]	34.3[3]	8.66	S	S

703 Noemi (2019-09-25)	12.5	0.15	0.37[3]	7.3[3]	200	
808 Merxia (2017-03-03)	9.8	0.15	0.21[3]	30.9[3]	30.63	L or S
913 Otila	12	0.15	0.28[3]	11.6[3]	4.87	S or Sq

[1] H magnitudes are derived from IRAS observations, when reported.

[2]Rotation periods are from the Lightcurve Data Base (Warren et al., 2021)

[3]NEOWISE (Masiero et al., 2014)

[4]IRAS (Tedesco et al., 2004)

[5]TRIAD (Zellner, 1979)

[6]Dunham and Herald (2006)

Table 4 continued: Physical & Orbital Properties

Object	*a (au)*	*e (degrees)*	*i (degrees)*	*Perihelion distance (au)*	*Aphelion distance (au)*	*Period (years)*
3 Juno	2.67	0.257	12.99	1.98	3.35	4.36
5 Astrea	2.57	0.191	5.37	2.08	3.07	4.13
6 Hebe	2.43	0.203	14.74	1.93	2.92	3.78
7 Iris (2018-12-13)	2.39	0.230	5.52	1.84	2.94	3.69
8 Flora	2.20	0.156	5.89	1.86	2.54	3.27
9 Metis	2.39	0.123	5.58	2.09	2.68	3.69
11 Parthenope	2.45	0.100	4.63	2.21	2.70	3.84
14 Irene (2019-10-03)	2.59	0.166	9.12	2.16	3.02	4.16
14 Irene (2020-02-03)	2.59	0.166	9.12	2.16	3.02	4.16
14 Irene (2017-02-15)	2.59	0.166	9.12	2.16	3.02	4.16
17 Thetis (2018-12-16)	2.47	0.133	5.59	2.14	2.80	3.88

17 Thetis (2019-05-15)	2.47	0.133	5.59	2.14	2.80	3.88
18 Melpomene	2.30	0.218	10.13	1.80	2.80	3.48
20 Massalia	2.41	0.143	0.71	2.07	2.75	3.74
30 Urania	2.37	0.128	2.10	2.06	2.67	3.64
33 Polyhymnia	2.87	0.332	1.85	1.92	3.83	4.87
39 Laetitia	2.77	0.112	10.37	2.46	3.08	4.61
63 Ausonia	2.40	0.127	5.78	2.09	2.70	3.71
67 Asia	2.42	0.185	6.03	1.97	2.87	3.77
82 Alkmene	2.76	0.220	2.83	2.15	3.37	4.59
103 Hera (2020-09-20)	2.70	0.079	5.42	2.49	2.92	4.44
115 Thyra	2.38	0.193	11.59	1.92	2.84	3.67
151 Abunditia	2.59	0.034	6.43	2.51	2.68	4.18
182 Elsa (2019-10-03)	2.42	0.187	2.01	1.97	2.87	3.76
182 Elsa (2020-09-26)	2.42	0.187	2.01	1.97	2.87	3.76
208 Lacrimosa	2.89	0.012	1.75	2.86	2.93	4.92
277 Elvira	2.88	0.092	1.16	2.62	3.15	4.90
352 Gisela	2.19	0.150	3.38	1.87	2.52	3.25
364 Isara	2.22	0.149	6.00	1.89	2.55	3.31
462 Eriphyla	2.87	0.088	3.19	2.62	3.13	4.87
703 Noemi	2.18	0.137	2.46	1.88	2.47	3.21
808 Merxia	2.75	0.129	4.72	2.39	3.10	4.55
913 Otila	2.20	0.171	5.81	1.82	2.57	3.26

Table 4: Description of derived mineralogy

Object	***S-type Subclass***	***Gaffey et al., (1993)***	***Inferred Mineralogy****	***Indicators***
3 Juno	SIV	SIV	L or LL chondrite	Indicated by Fa vs olivine abundance and Fs vs olivine abundance
5 Astrea	SIV		H chondrite	Indicated by Fa vs olivine abundance and Fs vs olivine abundance

6 Hebe	SIV	SIV	H chondrite	Indicated by Fa vs olivine abundance and Fs vs olivine abundance
7 Iris (2018-12-13)	SIV	SIV	LL chondrite	Indicated by Fa vs olivine abundance and Fs vs olivine abundance
8 Flora	n.a.			
9 Metis	SI	ungrouped	Olivine dominated	Strong Band I and weak Band II connoting minimal pyroxene.
11 Parthenope	SIII	SIV	clino-pyroxene bearing	greater pyroxene abundance compared to ordinary chondrite lithology
14 Irene (2019-10-03)	SI		Olivine dominated	Strong Band I and weak Band II connoting minimal pyroxene.
14 Irene (2020-02-03)	SIV		H chondrite	Indicated by Fa vs olivine abundance and Fs vs olivine abundance
Irene (2017-02-15)	SVI		Non-ordinary chondrite;	More olivine poor than Ordinary chondrites; less calcic pyroxene than SV asteroids
17 Thetis (2018-12-16)	SIV		H chondrite	Indicated by Fa vs olivine abundance and Fs vs olivine abundance
17 Thetis (2019-03-15)	SIV		Potentially primitive achondrite in the Acapulcoite-Lodranite Clan	Indicated by BI and BII centers (Lucas et al., 2019)
18 Melpomene	SVII	SV	Potentially either mesosiderite (metal + basaltic composition) or basaltic anorthositic composition.	Distinct Band I and Band II but weaker than basaltic achondrites and Vesta-type asteroids/HEDs. Potential mesosiderite analog, feldspar rich-basalt or metal-bearing V-type lithology

20 Massalia	SVI	SVI	Pyroxene dominated object (more olivine poor than ordinary chondrites)	More olivine poor than Ordinary chondrites; less calcic than SV asteroids
30 Urania	SIV		L Chondrite	Indicated by Fa vs olivine abundance and Fs vs olivine abundance
33 Polyhymnia	SVI	SIV	Pyroxene dominated object (more olivine poor than ordinary chondrites)	More olivine poor than Ordinary chondrites; less calcic than SV asteroids
39 Laetitia	SII		Ureilite composition	Olivine and clinopyroxene with greater abundance of olivne
63 Ausonia	SV	SIII	Calcic pyroxene and olivine	above olivine/pyrxene mixing line
67 Asia	SIV	SIV	H chondrite-like	Indicated by Fa vs olivine abundance and Fs vs olivine abundance
82 Alkmene	SIV	SVI	H chondrite-like	Indicated by Fa vs olivine abundance and Fs vs olivine abundance
103 Hera (2020-09-20)	SIV		H or L chondrite-like	Fa vs olivine abundance indicates an L-type lithology whole Fs vs. olivine abundance indicates either H or L-type.
115 Thyra (LXD)	n.a.	SIII	n.a.	n.a.
115 Thyra (prism)	SIV	SIII	H or L chondrite-like	Fa vs. olivine abundance indicates H chondrite lithology, while Fs vs. olivine abundances indicates either H or L chondrite
151 Abunditia	SV		Calcic pyroxene and olivine	above olivine/pyrxene mixing line; equal abundances of both minerals

182 Elsa (2019-10-03)	Basaltic achondrite			Basaltic achondrite
182 Elsa (2020-09-26)	SVI		Pyroxene dominated object (more olivine poor than ordinary chondrites)	More olivine poor than Ordinary chondrites; less calcic than SV asteroids
208 Lacrimosa	SVI		Pyroxene dominated object (more olivine poor than ordinary chondrites)	More olivine poor than Ordinary chondrites; less calcic than SV asteroids
277 Elvira	SIV		Potentially primitive achondrite in the Acapulcoite-Lodranite Clan	Indicated by BI and BII centers (Lucas et al., 2019)
352 Gisela	SII		Ureilite composition	Olivine and clinopyroxene with greater abundance of olivine
364 Isara	SIV	SII	LL chondrite-like	Indicated by Fa vs olivine abundance and Fs vs olivine abundance
462 Eriphyla	SIV		H chondrite-like	Indicated by Fa vs olivine abundance and Fs vs olivine abundance
703 Noemi (2019-09-25)	SIV		L or LL chondrite-like	Both Fa and Fs vs. olivine abundance indicate either an L or LL chondrite lithology.
808 Merxia (2017-03-03)	SVI		Pyroxene dominated object (more olivine poor than ordinary chondrites)	SVI

913 Otila	SIV	LL chondrite-like	More olivine poor than Ordinary chondrites; less calcic pyroxene than SV asteroids

*See Appendices 1 and 2 for more details.

Table 5: 3-µm Band Depth

Asteroid	*3-µm Band Depth*
3 Juno	n.a.
5 Astrea	1.87 ± 0.11
6 Hebe	1.73 ± 1.80
7 Iris (2018-12-13)	5.56 ± 0.97
8 Flora	1.26 ± 1.12
9 Metis	3.34 ± 1.5
11 Parthenope	1.02 ± 1.27
14 Irene (2019-10-03)	3.44 ± 0.25
14 Irene (2020-02-03)	5.21 ± 2.10
Irene (2017-02-15)	2.28 ± 0.64
17 Thetis (2018-12-16)	3.27 ± 1.81
17 Thetis (2019-05-15)	2.63 ± 0.6
18 Melpomene	3.02 ± 1.26
20 Massalia	3.02 ± 1.22
30 Urania	4.88 ± 2.92
33 Polyhymnia	3.78 ± 1.19
39 Laetitia	2.25 ± 4.05
63 Ausonia	3.28 ± 1.93
67 Asia	4.64 ± 1.45
82 Alkmene	2.45 ± 0.59
103 Hera (2020-09-20)	11.44 ± 4.6

115 Thyra	2.39± 0.56
151 Abunditia	4.53 ± 2.07
182 Elsa (2019-10-03)	1.99 ± 1.09
182 Elsa (2020-09-26)	2.34 ± 1.09
208 Lacrimosa	8.92 ± 2.85
277 Elvira	8.26 ± 1.37
352 Gisela	2.94 ± 1.09
364 Isara	2.78 ± 2.99
462 Eriphyla	10.36 ± 4.7
703 Noemi (2019-09-25)	3.32 ± 3.42
808 Merxia (2017-03-03)	5.29 ± 3.03
913 Otila	12.57 ± 1.52
115 Thyra (PRISM only)	n.a.

Table 6: Fit Statistics

parameter	*coef 1*	*coef 2*	*rmse*	*R*	*t*	*P*	*R^2*	*Comment*
perihelion distance	5.05	-6.49	2.38	0.46	2.84	0.008	0.212	Weak correlation
H magnitude	0.72	-1.53	3.81	0.42	2.57	0.0154	0.180	Weak correlation
diameter	-0.019	5.97	105.07	-0.378	-2.23	0.0334	0.142	Weak correlation
eccentricity	-17.78	6.94	4.25	-0.36	-2.13	0.0412	0.131	Weak correlation
period	1.95	-3.49	0.56	0.34	2.00	0.055	0.118	Weak correlation
semi major axis	4.53	-7.10	1.91	0.33	1.94	0.061	0.112	Weak correlation
Cross sectional area	-1.00E-04	5.17	13128	-0.32	-1.88	0.070	0.105	Weak correlation
eta	4.62	0.21	3.45	0.30	1.74	0.092	0.092	Weak correlation
heliocentric distance	3.04	-2.92	1.98	0.29	1.68	0.102	0.086	Negligible correlation
Flux (1/ semi-majr-axis^2)	-30.19	9.17	4.18	-0.28	-1.61	0.118	0.08	Negligible correlation
inclination	-0.21	5.43	4.16	-0.24	-1.36	0.185	0.058	Negligible correlation
T_eq	-0.02	9.59	269.16	-0.16	-0.87	0.393	0.026	Negligible correlation

phase	-0.07	4.69	6.15	-0.13	-0.74	0.464	0.018	Negligible correlation
delta	0.64	3.28	2.73	0.13	0.71	0.484	0.016	Negligible correlation
albedo	6.12	2.95	4.05	0.12	0.65	0.519	0.014	Negligible correlation
BAR	-0.65	5.05	3.52	-0.1	-0.53	0.600	0.01	Negligible correlation
Rotation Period (hours)	-0.007	4.43	41.01	-0.1	-0.54	0.592	0.01	Negligible correlation
Band II depth	-0.98	4.67	4.18	-0.08	-0.43	0.668	0.007	Negligible correlation
Aphelion distance	0.87	1.76	1.37	0.08	0.44	0.662	0.007	Negligible correlation
Band I center	-5.11	9.28	3.47	-0.07	-0.39	0.697	0.006	Negligible correlation
Band II center	-4.10	12.38	2.49	-0.07	-0.36	0.72	0.005	Negligible correlation
PCA Slope	-1.47	4.59	4.30	-0.04	-0.22	0.827	0.002	Negligible correlation
Band I depth	-0.69	4.46	4.35	-0.01	-0.04	0.965	0.0001	Negligible correlation

Table 7: H Ordinary chondrite-like asteroids

Asteroid	Sub-type*
5 Astrea	H Ordinary Chondrite-like
6 Hebe	H Ordinary Chondrite-like
14 Irene (2020)	H Ordinary Chondrite-like
17 Thetis (2018)	H Ordinary Chondrite-like
30 Urania	L Ordinary Chondrite-like
67 Asia	H Ordinary Chondrite-like
82 Alkmene	H Ordinary Chondrite-like
103 Hera	H or L Ordinary Chondrite-like
115 Thyra	H or L Ordinary Chondrite-like
462 Eriphyla	H Ordinary Chondrite-like

*Derivation of these sub-types described in **Appendix 2**.

Appendix Tables

A1.T1: Band Parameter Analysis Results

Asteroid	*BI Center (μm)*	*Band I Depth*	*Band II Center (μm)*	*Band II Depth*	*Band I Area*	*Band II Area*	*BAR*
3 Juno	0.958 ± 0.01	0.066 ± 0.001	1.987 ± 0.014	0.184 ± 0.001	0.031 ± 0.707	0.023 ± 0.0707	0.729 ± 0.1
5 Astrea	0.925 ± 0.01	0.043 ± 0.001	1.914 ± 0.013	0.02 ± 0.004	0.029 ± 0.707	0.032 ± 0.0707	1.095 ± 0.1
6 Hebe	0.931 ± 0.01	0.036 ± 0.002	1.914 ± 0.051	0.208 ± 0.002	0.018 ± 0.707	0.018 ± 0.0707	0.954 ± 0.1
7 Iris (2018-12-13)	1.008 ± 0.01	0.104 ± 0.001	1.956 ± 0.044	0.222 ± 0.001	0.036 ± 0.707	0.018 ± 0.0707	0.451 ± 0.1
9 Metis	1.066 ± 0.01	0.086 ± 0.001	2.169 ± 0.028	1.173 ± 0.001	0.026 ± 0.707	0.002 ± 0.0707	0.06 ± 0.1
11 Parthenope	0.957 ± 0.01	0.066 ± 0.001	1.947 ± 0.046	0.208 ± 0.001	0.035 ± 0.707	0.013 ± 0.0707	0.339 ± 0.1
14 Irene (2019-10-03)	0.928 ± 0.01	0.001 ± 0.002	1.951 ± 0.031	1.003 ± 0.001	0.013 ± 0.707	0.022 ± 0.0707	1.583 ± 0.1
14 Irene (2020-02-03)	0.919 ± 0.01	0.05 ± 0.0001	1.942 ± 0.038	0.178 ± 0.0001	0.025 ± 0.707	0.02 ± 0.0707	0.782 ± 0.1
14 Irene (2017-02-15)	0.919 ± 0.01	0.05 ± 0.0001	1.935 ± 0.038	0.178 ± 0.0001	0.025 ± 0.707	0.02 ± 0.0707	1.178 ± 0.1
17 Thetis (2018-12-16)	0.926 ± 0.01	0.043 ± 0.002	1.916 ± 0.053	0.29 ± 0.001	0.021 ± 0.707	0.021 ± 0.0707	0.946 ± 0.1
17 Thetis (2019-05-15)	0.926 ± 0.01	0.047 ± 0.005	1.876 ± 0.039	0.106 ± 0.001	0.023 ± 0.707	0.028 ± 0.0707	1.162 ± 0.1
18 Melpomene	0.914 ± 0.01	0.021 ± 0.002	1.984 ± 0.01	0.056 ± 0.003	0.009 ± 0.707	0.019 ± 0.0707	2.152 ± 0.1
20 Massalia	0.923 ± 0.01	0.051 ± 0.003	1.909 ± 0.038	0.137 ± 0.002	0.026 ± 0.707	0.031 ± 0.0707	1.176 ± 0.1
30 Urania	0.945 ± 0.01	0.042 ± 0.001	1.942 ± 0.043	0.225 ± 0.001	0.015 ± 0.707	0.013 ± 0.0707	0.828 ± 0.1
33 Polyhymnia	0.926 ± 0.01	0.061 ± 0.001	1.921 ± 0.036	0.175 ± 0.002	0.024 ± 0.707	0.031 ± 0.0707	1.26 ± 0.1
39 Laetitia	1.06 ± 0.01	0.106 ± 0.001	1.968 ± 0.019	0.221 ± 0.001	0.034 ± 0.707	0.019 ± 0.0707	0.517 ± 0.1
63 Ausonia	0.967 ± 0.01	0.102 ± 0.001	1.944 ± 0.046	0.309 ± 0.003	0.042 ± 0.707	0.026 ± 0.0707	1.091 ± 0.1
67 Asia	0.923 ± 0.01	0.055 ± 0.002	1.912 ± 0.042	0.177 ± 0.001	0.026 ± 0.707	0.029 ± 0.0707	1.085 ± 0.1
82 Alkmene	0.924 ± 0.01	0.059 ± 0.001	1.901 ± 0.028	0.072 ± 0.001	0.027 ± 0.707	0.034 ± 0.0707	0.976 ± 0.1
103 Hera	0.934 ± 0.01	0.042 ± 0.002	1.954 ± 0.023	0.181 ± 0.002	0.024 ± 0.707	0.023 ± 0.0707	0.916 ± 0.1
115 Thyra (PRISM only)	0.925 ± 0.01	0.06 ± 0.001	1.939 ± 0.033	0.169 ± 0.002	0.033 ± 0.707	0.027 ± 0.0707	0.794 ± 0.1
151 Abunditia	0.95 ± 0.01	0.092 ± 0.003	1.951 ± 0.034	0.561 ± 0.003	0.008 ± 0.707	0.01 ± 0.0707	1.164 ± 0.1
182 Elsa (2019-10-03)	0.921 ± 0.01	0.041 ± 0.002	1.937 ± 0.031	0.196 ± 0.001	0.017 ± 0.707	0.029 ± 0.0707	1.71 ± 0.1
182 Elsa (2020-09-26)	0.926 ± 0.01	0.048 ± 0.001	1.924 ± 0.033	0.123 ± 0.001	0.02 ± 0.707	0.03 ± 0.0707	1.481 ± 0.1

208 Lacrimosa	0.925 ± 0.01	0.031 ± 0.001	1.907 ± 0.052	0.179 ± 0.002	0.017 ± 0.707	0.023 ± 0.0707	1.309 ± 0.1
277 Elvira	0.931 ± 0.01	0.047 ± 0.001	1.889 ± 0.04	0.178 ± 0.002	0.023 ± 0.707	0.019 ± 0.0707	0.789 ± 0.1
352 Gisela	1.038 ± 0.01	0.128 ± 0.001	1.939 ± 0.046	0.364 ± 0.001	0.039 ± 0.707	0.018 ± 0.0707	0.439 ± 0.1
364 Isara	1.014 ± 0.01	0.14 ± 0.002	1.965 ± 0.026	0.346 ± 0.002	0.053 ± 0.707	0.023 ± 0.0707	0.43 ± 0.1
462 Eriphyla	0.932 ± 0.01	0.038 ± 0.001	1.943 ± 0.044	0.185 ± 0.001	0.018 ± 0.707	0.022 ± 0.0707	1.134 ± 0.1
703 Noemi	0.961 ± 0.01	0.141 ± 0.001	1.948 ± 0.025	0.303 ± 0.002	0.047 ± 0.707	0.023 ± 0.0707	0.466 ± 0.1
808 Merxia	0.925 ± 0.01	0.059 ± 0.002	1.912 ± 0.048	0.169 ± 0.001	0.025 ± 0.707	0.034 ± 0.0707	1.229 ± 0.1
913 Otila	0.977 ± 0.01	0.124 ± 0.003	1.933 ± 0.039	0.198 ± 0.004	0.054 ± 0.707	0.022 ± 0.0707	0.435 ± 0.1

A2.T1: Ordinary Chondrite Like Asteroids and modal mineralogy

Asteroid	*ol/ol+px*	*Modal abundance of fayalite*	*modal abundance of Ferrosilite*	*Sub-type designation*
3 Juno	0.56±0.03	26.27±1.3	22.43±1.4	L or LL
5 Astrea	0.48±0.03	19.77±1.3	17.90±1.4	H
6 Hebe	0.51±0.03	21.15±1.3	18.86±1.4	H
7 Iris	0.62±0.03	30.56±1.3	25.37±1.4	LL
14 Irene (2020)	0.55±0.03	18.42±1.3	16.95±1.4	H
(17) Thetis (2018)	0.51±0.03	20.11±1.3	18.14±1.4	H
30 Urania	0.54±0.03	24.05±1.3	20.88±1.4	L
67 Asia	0.49±0.03	19.45±1.3	17.68±1.4	H
82 Alkmene	0.51±0.03	19.56±1.3	17.75±1.4	H
103 Hera	0.52±0.03	21.85±1.3	19.35±1.4	H or L
115 Thyra	0.55±0.03	19.77±1.3	17.90±1.4	H or L
364 Isara	0.62±0.03	30.64±1.3	25.42±1.4	LL
462 Eriphyla	0.48±0.03	21.44±1.3	19.07±1.4	H
703 Noemi	0.61±0.04	26.75±1.3	22.76±1.4	L or LL
913 Otila	0.62±0.03	28.62±1.3	24.05±1.4	LL